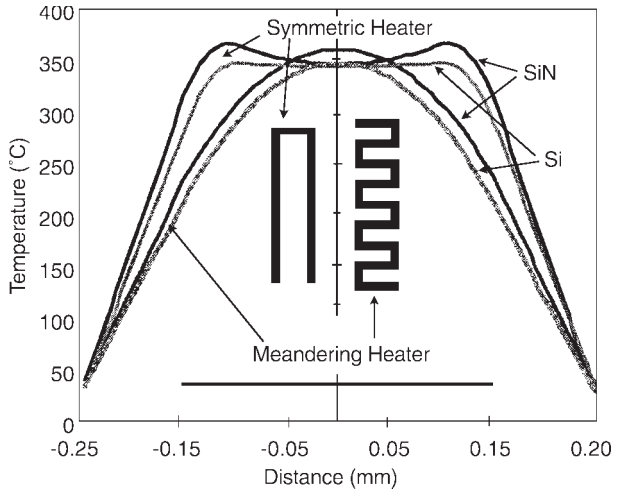

Figure 2.37 Temperature profiles across the membrane covering the reaction channel of the T micro reactor for a silicon and a silicon nitride membrane and two different heater designs, as discussed by Quiram et al. [128].

perature profile could be obtained. The obtained temperature profiles over the width of the reaction channel are displayed in Figure 2.37 for two different materials covering the channel. Attached to the cover membrane is a platinum heater, where one version thereof spans a considerable section of the channel width and the other version consists of strips located in both halves of the channel. The version with two heating strips apparently produces temperature profiles which qualify better to carry out reactions at a uniform temperature level.

2.6
Mass Transfer and Mixing

Similarly to heat transfer, fast mass transfer is one of the key aspects of micro reactors. Again, owing to the short diffusion paths, micro reactors permit a rapid mass transfer and a uniform solute concentration within the flow domain. Good control of reactant concentration throughout the whole reactor volume is a prerequisite for highly selective chemical reactions and helps to avoid hazardous operation regimes. In addition, overcoming mass transfer limitations by rapid mixing allows the exploitation of the rapid intrinsic kinetics of chemical reactions and allows a higher yield and conversion. However, when dealing with liquid-phase reactions, fast mixing remains a challenge even at length scales of 100 μm or less owing to the small diffusion constants in liquids.

Chemical Micro Process Engineering: Fundamentals, Modelling and Reactions
Volker Hessel, Steffen Hardt, Holger Löwe

ISBN: 3-527-30741-9

2.6.1 Transport Equation for Species Concentration

The governing equation for mass transport in the case of an incompressible flow field is easily derived from the general convection–diffusion equation Eq. (32) with $\Phi = c$ and is given by

$$\frac{\partial c}{\partial t} + u_i \frac{\partial c}{\partial x_i} = \frac{\partial}{\partial x_i}\left(D \frac{\partial c}{\partial x_i} \right) - r \,, \tag{89}$$

where c is the concentration of a solute in units of mol/volume, u_i the flow velocity, D the molecular diffusivity and r a source term due to chemical reactions. For a given velocity field and a vanishing source term, the solution of Eq. (89) is governed by a single dimensionless group, which is the Peclet number:

$$\mathrm{Pe} = \frac{u\, d}{D} \,. \tag{90}$$

In this expression, u is a typical velocity scale and d a typical length scale, for example the diameter of a micro channel. The Peclet number represents the ratio of the diffusive and the convective time-scales, i.e. flows with large Peclet numbers are dominated by convection.

2.6.2 Special Numerical Methods for Convection-Dominated Problems

As already indicated in Section 2.3.1, the numerical solution of convection–diffusion equations such as Eq. (89) is often impaired by numerical diffusion. From Eq. (42), it is obvious that for the upwind scheme the dimensionless group determining the strength of numerical diffusion is the cell-based Peclet number, i.e. the Peclet number to which the dimension of a grid cell enters as a length scale. When considering mass transfer in gases, the cell size can often be chosen small enough to suppress numerical diffusion artefacts. However, for mass transfer in liquids this is often not possible owing to the molecular diffusion constant, which is about three orders of magnitude smaller.

The solution of a pure convection equation for a scalar field Φ:

$$\frac{\partial \Phi}{\partial t} + \frac{\partial (u_i \Phi)}{\partial x_i} = 0 \tag{91}$$

can be regarded as a benchmark problem for the validation of corresponding numerical schemes. Considering a constant velocity field u_i and an initial distribution $\Phi(t = 0)$, Eq. (91) describes the displacement of this distribution along the streamlines of the flow. Apart from such a displacement, the distribution of the scalar field remains undisturbed. A numerical solution usually cannot reproduce this behavior, rather some distortion and a dispersion of the field distribution will be induced. In order to shed more light on the numerical structure of the problem,

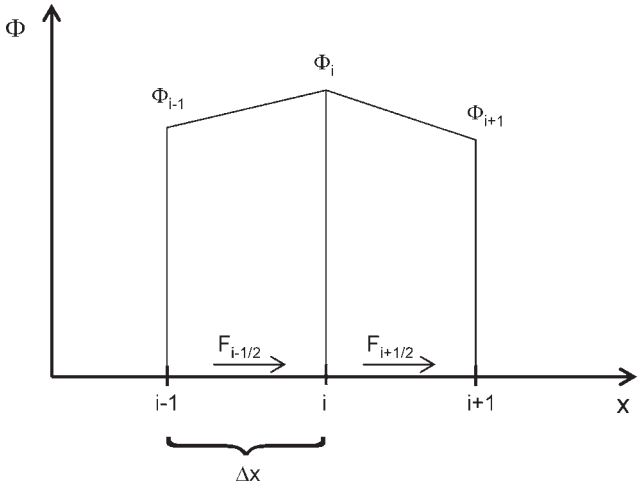

Figure 2.38 Finite-difference grid for the solution of the one-dimensional convection equation. The $F_{i\pm1/2}$ denote the fluxes from node i to the neighboring nodes.

consider a one-dimensional version of Eq. (91) discretized on a finite difference grid as shown in Figure 2.38 Based on first-order explicit time differencing, the discretized version of the convection equation can be written in the general form

$$\Phi_i^{n+1} = \Phi_i^n - \frac{F_{i+1/2} - F_{i-1/2}}{\Delta x}, \tag{92}$$

where the superscripts refer to the temporal and subscripts to the spatial coordinates. The $F_{i\pm1/2}$ are the fluxes between node i and its neighboring nodes which effect an increase or decrease of Φ_i in the next time step. They are in general a function of the values of Φ at different node locations, depending on the specific differencing scheme used. In stable discretization schemes, the fluxes usually have a diffusive component which damps off fluctuations. An undesired side effect of such numerical diffusion is that it also disperses the real, physical concentration peaks. In contrast, diffusion-free schemes such as central differencing may lead to instabilities, since unphysical over- and undershoots and new maxima and minima of the solution field are produced.

In order to minimize numerical diffusion, Boris and Book [131] formulated the idea of blending a low-order stable differencing scheme with a higher order, potentially unstable, scheme in such a way that steep concentration gradients are maintained as well as possible. The algorithm they proposed consists of the following steps:

- Compute an approximation of the solution at the next time step using a low-order scheme (indicated by superscript L):

$$\tilde{\Phi}_i^{n+1} = \Phi_i^n - \frac{F_{i+1/2}^{\mathrm{L}} - F_{i-1/2}^{\mathrm{L}}}{\Delta x}. \tag{93}$$

- Based on a higher order scheme (indicated by superscript H), compute 'anti-diffusive' fluxes:

$$A_{i\pm1/2} = F^{\mathrm{H}}_{i\pm1/2} - F^{\mathrm{L}}_{i\pm1/2}\,. \tag{94}$$

- Multiply $A_{i\pm1/2}$ with a flux limiter:

$$A^{\mathrm{C}}_{i\pm1/2} = C_{i\pm1/2}\; A_{i\pm1/2}\,. \tag{95}$$

- Add the limited antidiffusive fluxes to the approximate solution

$$\Phi^{n+1}_i = \tilde{\Phi}^{n+1}_i - \frac{A^{\mathrm{C}}_{i+1/2} - A^{\mathrm{C}}_{i-1/2}}{\Delta x}\,. \tag{96}$$

Without the third step, the multiplication with the flux limiter, addition of the antidiffusive fluxes would just remove the terms causing diffusion from the approximate solution obtained with the low-order scheme. However, such a simple correction would usually result in an unstable numerical scheme. For this reason, the flux limiter $C_{i\pm1/2}$ is chosen such that the antidiffusion stage generates no new maxima or minima of Φ and does not accentuate already existing extrema. The choice of the flux limiter is crucial for the quality of the numerical approximation. Effectively, the procedure described above can be regarded as switching between high- and low-order approximations adaptively depending on the smoothness of the solution. The potentially unstable high-order approximation is used in regions where owing to the structure of Φ, an instability cannot be created.

Methods based on the addition of antidiffusive fluxes to a low-order differencing scheme are termed flux-corrected transport (FCT) algorithms. A multidimensional version of a FCT method was first developed by Zalesak [132]. The quality of corresponding numerical schemes is usually assessed by solving benchmark problems such as the convection of a rectangular pulse. For a considerable number of such examples, it has been shown that FCT methods are able to preserve steep gradients and stepwise changes of the solution field much better than standard differencing schemes [131, 132].

2.6.3 Mixing Channels

In the literature, a variety of different micro mixing devices have been described [133], most of which operate in the laminar flow regime. In order to understand the dynamics of micro mixers and to determine optimized designs, modeling and simulation techniques were applied in some cases. The simplest micro mixer is the so-called mixing tee which is displayed on the top of Figure 2.39. Two inlet channels merge into a common mixing channel where mixing of the two co-flowing fluid streams occurs. The mixing characteristics of T-type mixers was investigated by Gobby et al. [134] using CFD methods. Mixing of gases in a channel of 500 µm width was considered and certain geometric parameters such as the aspect

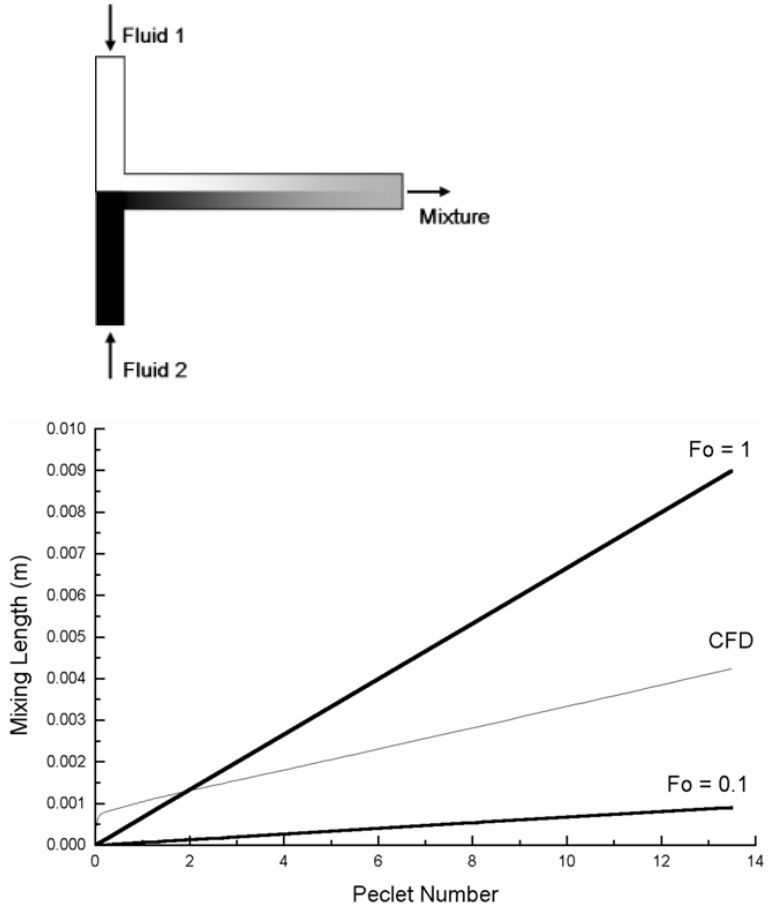

Figure 2.39 Schematic design of a mixing tee (above) and CFD results for mixing of gases in a channel of 500 µm width and 300 µm depth, taken from [134] (below).

ratio of the mixing channel or the angle at which the two inlet channels meet were varied. In order to quantify mixing, a mixing length was defined as the length in flow direction after which the gas composition over all positions of a channel cross-section deviates by no more than 1% of the equilibrium composition. The CFD results for the mixing length as a function of Peclet number are displayed on the right side of Figure 2.39.

In addition to the CFD results, estimates of the mixing length based on the Fourier number:

$$\mathrm{Fo} = \frac{D\,t}{l^2} \tag{97}$$

are shown in Figure 2.39. The Fourier number relates a residence time t in the mixing channel to the binary diffusion constant and a characteristic length scale l,

which is the width of the channel. For a given value of Fo and a given flow rate, the length along the mixing channel necessary to achieve the corresponding Fourier number was determined. As is apparent from Figure 2.39, the Fourier number is a reasonable indicator for mixing which occurs for Fourier numbers between 0.1 and 1.0. The linear increase of the CFD-based mixing length as a function of Peclet number points to a very simple mixing mechanism via diffusion between co-flowing fluid lamellae. Obviously, complex convection-dominated mixing mechanisms (for example driven by swirls or recirculating flows) are absent in the simple mixing-tee configuration for the range of Peclet numbers studied.

Microfluidic mixing tees are useful for the processing of species with high diffusion constants at comparatively low volume flows. However, for mixing of liquids at only moderate volume flows, more elaborate micro mixing concepts are needed. The next level of complexity in micro mixer design is to go from a straight mixing channel to a curved channel or a channel with structured walls. In that context, a design that has been studied in some detail is a zigzag micro channel, the geometry of which is shown in Figure 2.40. Mengeaud et al. [135] studied mixing in zigzag micro channels in a 2-D finite-element model and conducted experiments using fluorescein to visualize the mixing process. In order to suppress artefacts from numerical diffusion, the Peclet number of the flow was fixed at moderate values (Pe = 2600). When the flow velocity was varied, the diffusion constant was varied along with it in order to keep the Peclet number fixed. Owing to this fact, diffusion constants of up to 10^{-6} m^2 s^{-1} were used, three orders of magnitude larger than typical liquid diffusion constants. Several channel geometries with varying widths of the order of 100 µm and varying periods of the zigzag structures were considered. The configuration with maximum mixing efficiency was studied in more detail and exhibits an interesting behavior when the Reynolds number is increased. For Reynolds numbers up to 80 the mixing efficiency is equal to an equivalent straight mixing channel, indicating that convective mixing effects are negligible. For larger Reynolds numbers an increase of the mixing efficiency sets in, indicating that the flow pattern changes and convective mass transfer promotes mixing. Specifically, recirculation zones as shown on the right side of Figure 2.40 begin to form. Hence, for comparatively large Reynolds numbers, zigzag mixing channels achieve a distinctively higher mixing efficiency than straight channels.

Figure 2.40 Zigzag micro mixer with concentration field (left) and flow stream lines (right) obtained from a CFD simulation for a Reynolds number of 38. In [135] a sawtooth geometry of larger amplitude was considered and distinctive recirculation zones were found only at Reynolds numbers larger than 80.

This observation is supported by experiments carried out with a phosphate buffer and a fluorescein solution for visualization of the mixing process. However, in the experiments there are indications that the critical Reynolds number where the mass transfer enhancement sets in is lower (~7) than predicted by the simulations, a fact which is not well understood.

Another strategy to promote the mixing of two fluid streams merging in a channel is to induce a helical flow which redistributes the fluids in the mixing channel. Stroock et al. [136, 137] described a method to induce helical flows in straight channels. As a fundamental principle to induce recirculating flow patterns they considered the flow over grooved surfaces. Their theoretical studies were done for a slab geometry where one boundary is a sinusoidally modulated surface [136]. By writing down a perturbation series in the amplitude of the sinusoidal grooves they were able to solve the Stokes equation for flow parallel and perpendicular to the grooves. By a linear superposition of the two specific solutions, the general solution for an arbitrary flow direction is obtained. It turns out that on length scales large compared with the amplitude and the inverse wavenumber of the sinusoidal modulations, the grooved surface can be regarded as inducing a slip flow the direction of which in general does not coincide with the direction of the pressure gradient. The slip velocity u_i is obtained from a boundary condition of the form

$$u_i\big|_{z=0} + (Z_{\text{eff}})_{ij} \left.\frac{\partial u_j}{\partial z}\right|_{z=0} = 0 \tag{98}$$

on the grooved surface. The 2×2 tensor Z_{eff} depends on the applied pressure gradient and the orientation of the grooves in the surface located at $z = 0$. When at least one of the walls of a micro channel contains grooves standing at an angle θ to the main flow direction, a situation as depicted in Figure 2.41 is encountered. Owing

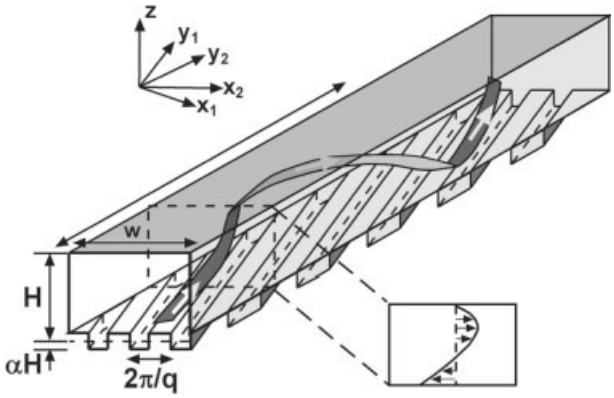

Figure 2.41 Schematic diagram of a micro channel with grooves in the bottom wall, taken from [136]. The ribbon indicates a typical streamline in the channel. In the box at the bottom the velocity profile over a channel cross-section is drawn schematically.

to the slip flow not being aligned with the pressure gradient along the channel, a helical flow is induced with helices extending over the entire cross-section of the channel.

For micro mixing applications, a helical flow would allow one to increase the interfacial area between the two fluid lamellae to be mixed, but it would usually not effect a dramatic improvement of mixing efficiency. Aref [138] showed that two vortex structures need to be superposed in an alternating fashion in order to create a chaotic flow pattern ('blinking vortex flow'). The corresponding flow can be described mathematically as a non-integrable Hamiltonian system. Aref computed the distribution of tracer particles by the blinking vortices in the chaotic regime and was able to show that the particles spread over the entire flow domain after some cycles.

In order to realize the blinking vortex flow principle in a mixing channel, Stroock et al. proposed to use a periodic, staggered arrangement of grooves to induce a chaotic flow pattern even at low Reynolds numbers [137]. The corresponding mixer geometry is shown in Figure 2.42. The bottom of the channel of height h and width w contains a staggered arrangement of grooves, where a fraction p of the lower channel wall has grooves inducing a left-handed recirculation and the remaining wall fraction induces a right-handed recirculation. A schematic view of the channel cross-section is shown on top of Figure 2.42. If $p \neq 1/2$, the vortex pattern is asymmetric, and a superposition of two patterns exhibiting the larger of the two vortices on the left and right sides, respectively, could result in chaotic flow. The superposition is achieved by the alternating, staggered groove patterns shown in Figure 2.42. The lower part of the figure shows channel cross-sections with two streams of fluorescent and clear solutions after 0, 0.5 and 1 cycle. The images were recorded using a confocal microscope. The two different vortices are clearly visible and the third

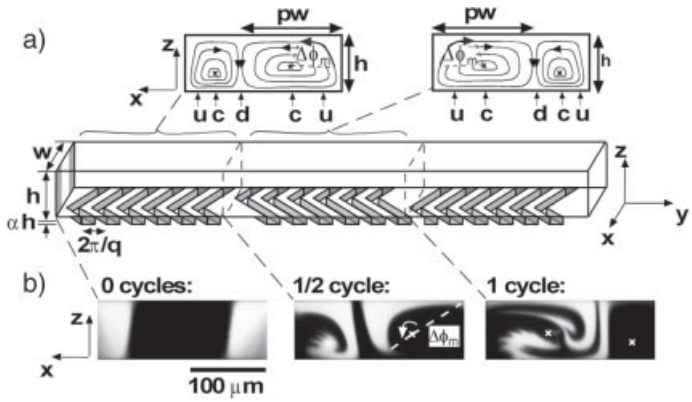

Figure 2.42 Micro mixer geometry with staggered groove structures on the bottom wall, as considered in [137]. The top of the figure shows a schematic view of the channel cross-section with the vortices induced by the grooves. At the bottom, confocal micrographs showing the distribution of two liquids over the cross-section are displayed.

frame shows first indications of a chaotic disturbance of the flow. By analyzing the gray-scale distribution of their confocal micrographs, Stroock et al. were able to show that chaotic mixing occurs in their mixer comprising a staggered arrangement of grooves. An indication of the chaoticity of the mixing process is the mixing length which was found to scale as ln Pe.

The theoretical results obtained by Stroock et al. are based on the Stokes flow regime and rely on surface modulations of comparatively small amplitude. Schönfeld and Hardt [139] studied helical flows in micro channels by numerically solving the full Navier–Stokes equation for different channel geometries including channels with corrugated walls. They compared the transversal velocities due to the helical flow to the analytical results and found good agreement even for grooves almost as deep as the channel itself.

Furthermore, as an alternative principle to induce helical flows, they studied the Dean effect as described in Section 2.4.3. In contrast to the single vortex induced by simple grooved channel walls, in curved channels at least two counter-rotating vortices are formed. Schönfeld and Hardt showed that in the curved micro channels considered, the transverse velocities due to the vortex-like structures are of comparable order of magnitude to those obtained with grooved channel walls. Typical results obtained from the numerical solution of the convection–diffusion equation for the concentration field are displayed in Figure 2.43. The left side of the figure shows the channel geometry, where typical dimensions are $a = 200$ µm and $R = 1000$ µm. On the right side the evolution of two initially vertical fluid lamellae

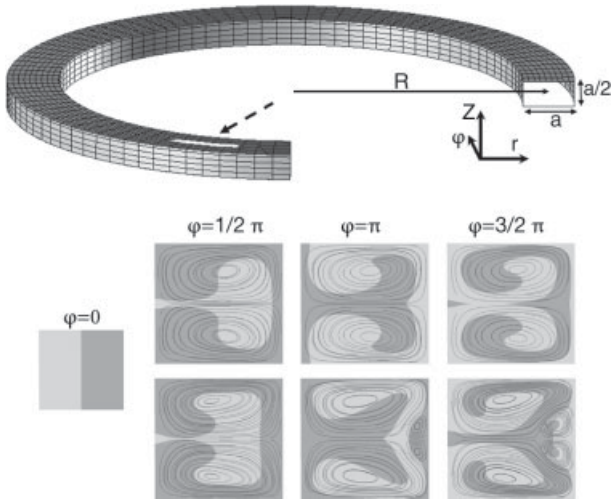

Figure 2.43 Model geometry for the CFD calculations on flow in curved micro channels (above) and time evolution of two initially vertical fluid lamellae over a cross-section of the channel (below), taken from [139].The secondary flow is visualized by streamlines projected on to the cross-sectional area of the channel. The upper row shows results for $K = 150$ and the lower row for $K = 300$.

for a vanishing diffusion constant is displayed, in the upper row for a Dean number of $K = 150$ and in the lower row for $K = 300$. Depending on the Dean number, a flow pattern with either two or four counter-rotating vortices is found.

In order to permit efficient mixing, a chaotic flow pattern would be desirable. Schönfeld and Hardt suggested a method to realize a version of the blinking vortex principle in curved channels [139]. By a periodic arrangement of channel sections of different hydraulic diameters, the two- and the four-vortex pattern could be generated in an alternating sequence, thus effecting a stretching and folding of the fluid lamellae in a chaotic manner. Alternatively, at Dean numbers high enough for the four-vortex pattern to emerge, a periodic sequence of channel sections of alternating curvature could allow switching between flow patterns with the two small vortices either on the left or on the right side of the channel cross-section.

2.6.4 Estimation of Mixing Efficiency by Flow-field Mapping

For flows created in channels which exhibit a certain periodicity, due either to alternating groove patterns in the walls or to alternating curved sections, there is an elegant method to compute the growth of interfacial area per spatial period and to estimate the mixing efficiency. By the fluid streamlines, each point of a channel cross-section (x_k, y_k) is mapped to another point (x_{k+1}, y_{k+1}) of the corresponding cross-section after one period of the fluidic structures, as shown in Figure 2.44. Such a so-called Poincaré map can be written formally as

$$(x_{k+1}, y_{k+1}) = P[(x_k, y_k)]\,. \tag{99}$$

The function P can be computed from either an analytical or a numerical representation of the flow field. In such a way, a 3-D convection problem is essentially reduced to a mapping between two-dimensional Poincaré sections. In order to analyze the growth of interfacial area in a spatially periodic mixer, the initial distri-

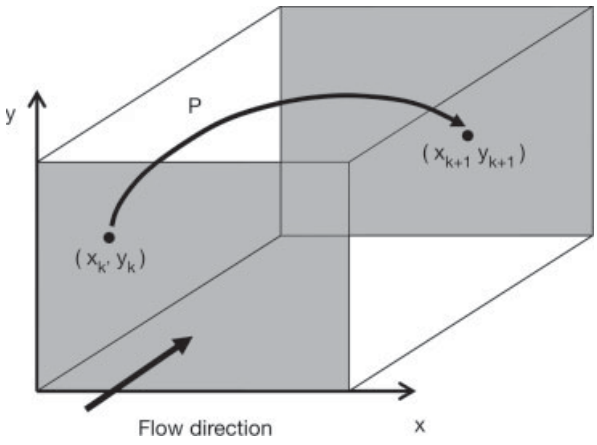

Figure 2.44 Section of a mixing channel with a map P connecting the points of two cross-sectional planes.

bution of fluids may be represented as a set of grid cells or points distributed over the inlet patch and tagged with different colors according to binary concentration values. By successively applying the mapping of Eq. (99) the points are redistributed or the grid cells are tagged with different colors. In such a way the growth of interfacial area and the stretching and folding of fluid lamellae can be analyzed. The Poincaré map method was applied by Linxiang et al. [140] to study mixing in curved channels.

2.6.5 Multilamination Mixers

Usually, even with zigzag mixing channels or chaotic mixers, liquid micro mixing can only be completed at moderate volume flows. In chemical process technology, throughput is often an important issue, and for this reason micro mixer designs going beyond the concept of two streams merging in a single mixing channel are needed. When abandoning mixer architectures where the fluid streams to be mixed are guided through only a single layer and going to multilayer architectures, the principle of multilamination becomes accessible. In multilamination mixers the two fluid streams are split into a multitude of sub-streams which are subsequently merged to form an interdigital arrangement of fluid lamellae. A design of a multilamination mixer is shown on the left side of Figure 2.45. From the flow distribution zone an interdigital arrangement of fluid lamellae enters a constriction with a width of 500 µm where the width of the lamellae is decreased, a principle known as hydrodynamic focusing. Subsequently the fluid streams enter a constriction which opens up to a wider channel.

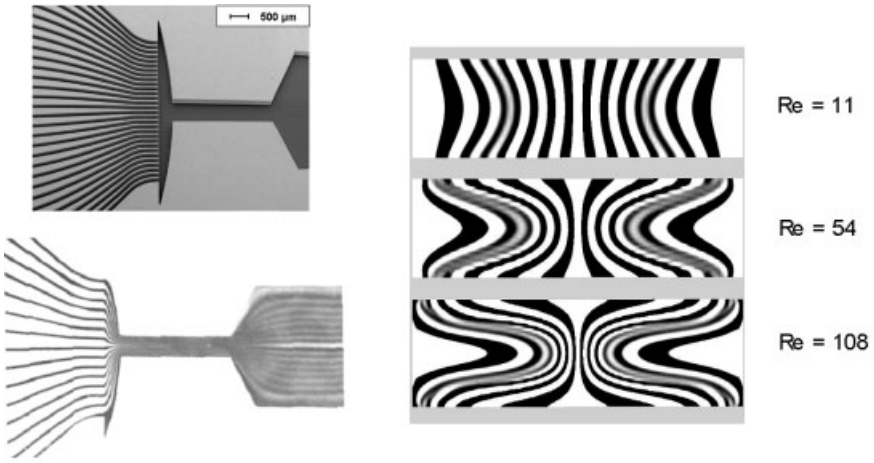

Figure 2.45 Design of a multilamination mixer with hydrodynamic focusing (upper left) and flow pattern in such a mixer for a total volume flow of 10 ml h^{-1} of water (lower left), taken from [141]. The right side of the figure shows the orientation of liquid lamellae over a cross-section of the constriction for different Reynolds numbers [142].

Hessel et al. [141] studied mixing in interdigital micro mixers experimentally, where different degrees of hydrodynamic focusing and mixers with and without opening of the constriction to a wider channel were considered. A result of such an experiment at a total volume flow of 10 ml h^{-1} is displayed at the lower left of Figure 2.45. Pure water and water colored with a dye were used as liquids. Apparently, it can be deduced that mixing has not proceeded to any sufficient degree, since the different colors are still visible in the reopening section. When the volume flow is increased substantially, downstream from the center of the constriction an average color becomes visible. Such a result could possibly be interpreted as complete mixing, but CFD simulations performed for this mixer geometry [142] offer a different explanation.

The CFD simulations were done in a 3-D model of the mixer based on the finite-volume method. Owing to artefacts from numerical diffusion occurring at high Peclet numbers, it was not possible to obtain satisfactory solutions of the convection–diffusion equation for typical liquid diffusion constants. In order to study the flow patterns in the mixer, a streamline-tracking technique was employed. From the velocity field obtained as solution of the Navier–Stokes equation, the flow streamlines were determined by numerical integration starting at the interface from the flow distribution zone to the actual mixer. The streamlines corresponding to pure and dyed water were tagged with a different color. By this means it is possible to compute flow patterns such as the one displayed on the right in Figure 2.45, which however, do not incorporate effects of diffusive mass transport. The diagram shows a cross-section through the constriction of the mixer for different Reynolds numbers. For small Reynolds numbers, the fluid lamellae are mainly oriented vertically. When the Reynolds number increases, the lamellae become deformed and assume a U-shape. This explains why at high flow rates a uniform color is observed in the mixing zone: a light beam cutting vertically through the flow domain intersects lamellae of different color, thus averaging out the coloring of the two different liquids. Hence it follows that experimental techniques for characterizing multilamination mixing processes based on the diffusion of a dye have to be viewed with care.

The streamline-tracking technique allows the extraction of qualitative information on the flow patterns in micro mixers, but does not permit a quantitative prediction of mixing efficiency. When hydrodynamic focusing does not proceed as rapidly as in the mixer displayed in Figure 2.45, the distortion of liquid lamellae is less pronounced and a semi-analytical method can be used to predict the efficiency of multilamination micro mixers, as proposed by Hardt and Schönfeld [142]. Approximately, a mixing process can be viewed as a pure diffusion process in a frame of reference co-moving with the average velocity of the flow. The solution of the diffusion equation for an initial condition being defined as a parallel, interdigital arrangement of liquid lamellae of width L and concentration values of 0 and 1 can be written as

$$c(x,t) = \frac{1}{2} + \sum_{n=1,3,\ldots} \frac{2}{n\,\pi} (-1)^{\frac{n-1}{2}} \exp(-D\,k_n^2\,t) \cos(k_n\,x)\,, \tag{100}$$

where D is the diffusion constant and $k_n = n\pi/L$. On the basis of Eq. (100), the concentration field at different positions in the mixing channel of a multilamination mixer can be computed approximately. Hardt and Schönfeld used this approach to compare the mixing efficiency of different multilamination mixers and to design a new mixer allowing for a very high throughput and short mixing times [142].

2.6.6 Active Micro Mixing

In chemical micro process technology there is a clear dominance of pressure-driven flows over alternative mechanisms for fluid transport. However, any kind of supplementary mechanism allowing promotion of mixing is a useful addition to the toolbox of chemical engineering. Also in conventional process technology, actuation of the fluids by external sources has proven successful for process intensification. An example is mass transfer enhancement by ultrasonic fields which is utilized in sonochemical reactors [143]. There exist a number of microfluidic principles to promote mixing which rely on input of various forms of energy into the fluid.

The large surface-to-volume ratio of micro flows suggests the use of an actuation mechanism based on surface forces. One suitable mechanism is electroosmotic flow which is induced due to the force that an external electric field exerts on the electric double layer (EDL) building up at a solid/liquid interface. The extension of the EDL is usually very small compared with the width of a micro channel and the electroosmotic flow can be modeled by the Helmholtz–Smoluchowski slip-flow boundary condition Eq. (21). The zeta potential ζ determines the magnitude and direction of the electroosmotic flow close to the solid surface. Among other factors, ζ depends on the electric potential of the surface. An electric field normal to the solid/liquid interface can be imposed with the aid of electrodes embedded in the channel walls. In such a way, it is possible to reverse the direction of the electroosmotic flow building up in a micro channel. For this purpose, an electric field along the axis of the channel is created. A field perpendicular to the channel walls due to the embedded electrodes is used to tune the zeta potential. The direction of the flow induced by the driving electric field then depends on the potential of the electrodes. When using arrays of electrodes embedded in the upper and lower walls of a micro channel, periodic recirculating flow patterns can be generated. A possible electrode arrangement (represented by black rectangles) together with streamlines of flow patterns emerging in such channels is depicted on the left side of Figure 2.46.

Qian and Bau [144] have analyzed such electroosmotic flow cells with embedded electrodes on the basis of the Stokes equation with Helmholtz–Smoluchowski boundary conditions on the channel walls. They considered electrode arrays with a certain periodicity, i.e. after k electrodes the imposed pattern of electric potentials repeats itself. An analytic solution of the Stokes equation was obtained in the form of a Fourier series. Specifically, they analyzed the electroosmotic flow patterns with regard to mixing applications. A simple recirculating flow pattern such as the one

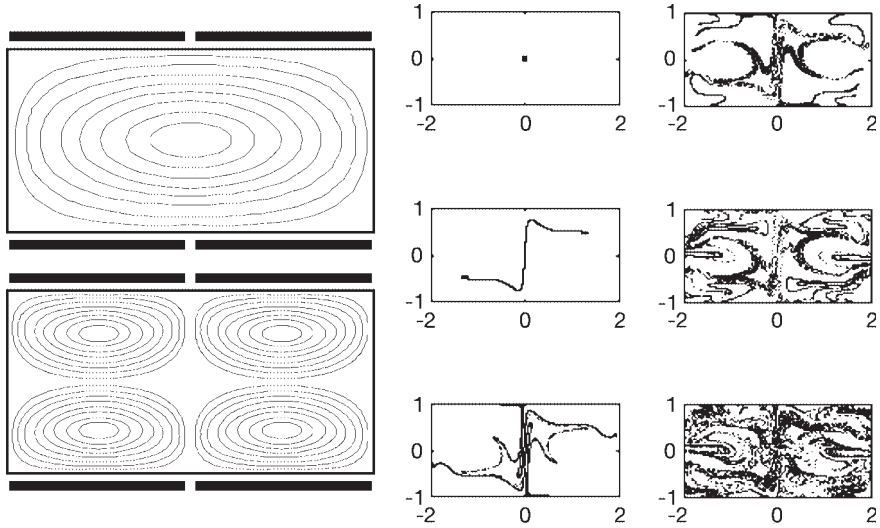

Figure 2.46 Section of a micro channel with electrodes embedded in the channel walls (left). When an electric field is applied along the channel, different flow patterns may be created depending on the potential of the individual electrodes. The right side shows the time evolution of an ensemble of tracer particles initially positioned in the center of the channel for a flow field alternating between the single- and the four-vortex pattern shown on the left [144].

shown on left side of Figure 2.46 will not promote mixing substantially, since tracer particles with a small diffusivity will follow the streamlines, while transport transverse to the streamlines will be negligible. In order to speed up mixing, an alternating flow created by switching between the single-vortex and the four-vortex pattern shown on the left side of Figure 2.46 was considered. Inertial effects were neglected and it was assumed that for the first half of the switching cycle T the flow is given by the single-vortex pattern, whereas for the second half of the cycle the four-vortex pattern prevails. With the flow pattern given, the time evolution of an ensemble of massless particles can be computed by integration along the streamlines. Qian and Bau positioned a small blob of massless particles in the center of the flow cell and computed their trajectories by solving the kinematic equations numerically. Their numerical results for times between 0 and 15T are displayed on the right side of Figure 2.46 The tracer particles spread over the volume of the cell in a chaotic manner and filled almost the complete cell volume in the final frame. The results suggest that chaotic advection based on alternating electroosmotic flows is a powerful principle for mixing of chemical species with a small diffusion constant. The principle suggests itself especially for fluidic cells with a slowly flowing liquid or a liquid at rest.

An electroosmotic mixer allowing to enhance the efficiency of mixing tees was proposed by Meisel and Ehrhard [145]. The corresponding geometry with a cylinder in the center of a mixing channel is displayed on top of Figure 2.47. When mixing ionic liquids, an electric double layer will form above the solid/liquid inter-

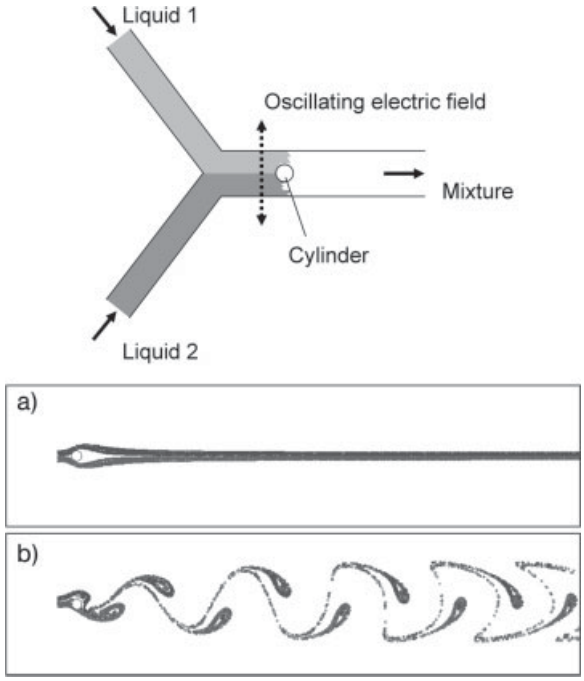

Figure 2.47 Micro mixer based on the excitation of an electro-osmotic flow around a cylinder by an oscillatory electric field (top). The bottom of the figure shows particle traces on both sides of the liquid/liquid interface with no electric field (above) and with the electric field switched on (below), as described in [145].

faces including the surface of the cylinder. An oscillatory electric field applied perpendicular to the channel in the region of the cylinder induces an electroosmotic flow around the cylinder perpendicular to the main flow along the mixing channel which may be pressure driven. Meisel and Ehrhard studied the performance of such cylindrical mixing structures by solving the Navier–Stokes equation in the channel numerically using a finite-element approach. The electroosmotic flow on the surface on the cylinder was modeled by imposing the Helmholtz–Smoluchowski slip-flow boundary condition. Characteristic results of these simulations are displayed on the bottom of Figure 2.47. The diagrams show the paths of massless particles on both sides of the interface separating the two liquids (which is not an interface in the strict sense since the liquids are miscible). In the upper diagram, the electric field is switched off and the particles follow a straight path. In the lower diagram a vortex street is created due to the oscillatory electroosmotic flow. Such vortex structures increase the interfacial area between the two liquids and promote mixing. A more quantitative analysis of the mixing efficiency and an optimization of the mixing device based on an arrangement of multiple cylinders requires further studies.

An alternative mechanism allowing promoting mass transfer between two liquids that has been studied in some detail is magneto-hydrodynamic mixing. The idea is based on flow patterns originating from the force an external magnetic field exerts on ions moving in a liquid. In order to induce a motion of the ions, electrodes are integrated in a micro channel which create an electrophoretic current when a voltage is applied. When an external magnetic field acts on the moving ions, they experience a Lorentz force driving them to a direction orthogonal to their momentary velocity and orthogonal to the magnetic field and drag the surrounding liquid molecules along with them. In short, the magneto-hydrodynamic forces are implemented by adding a source term

$$\left(\mathbf{J} \times \mathbf{B}\right)_i \tag{101}$$

which is the cross product of the current density of the ions and the magnetic field to the Navier–Stokes equation Eq. (16). The current density is given by

$$J_i = \sigma \left[E_i + (\mathbf{u} \times \mathbf{B})_i\right], \tag{102}$$

where σ is the conductivity of the liquid, E_i the electric field strength and u_i the fluid velocity.

On top of Figure 2.48 a schematic design of a magneto-hydrodynamic mixer as proposed by Bau et al. [146] is displayed. The mixer consists of a micro channel of width w and depth $2h$ and contains electrodes separated by a distance L. A DC voltage is applied in such a way that the potential alternates between + and – for neighboring electrodes. Orthogonal to the channel a magnetic field is applied. In their theoretical treatment, Bau et al. exploited the symmetry of the problem and considered only the section of the channel enclosed by the gray faces. The rectangular patches orthogonal to the channel walls intersect the centerline between two electrodes. Based on the assumptions $h << w$ and $h << L$, they were able to obtain an approximate solution of the Navier–Stokes equation in the form of a series expansion. Their solution describes the flow in a static electric field along the channel and a static magnetic field perpendicular to the channel. The corresponding evolution of the interface between two liquid lamellae initially oriented in the x direction and each filling half of the channel is displayed on the bottom of Figure 2.48. Each of the diagrams shows a x–y section through the computational domain and the different diagrams are labeled with a time coordinate nondimensionalized by a characteristic time-scale of the system. By the magneto-hydrodynamic forces a vortex flow is induced which causes an entanglement of the liquid lamellae. In a pure diffusion process without convection, mass transfer between the lamellae is governed by a $t^{1/2}$ law. In the magnetohydrodynamic mixer of Bau et al., the interfacial area is found to increase approximately linearly with time, an effect which superposes diffusion and effects a substantial reduction in mixing times. However, the linear interfacial stretching falls short of chaotic advection which exhibits an exponential growth as a function of time. In experiments conducted with a prototype system, the theoretical results were confirmed qualitatively [146].

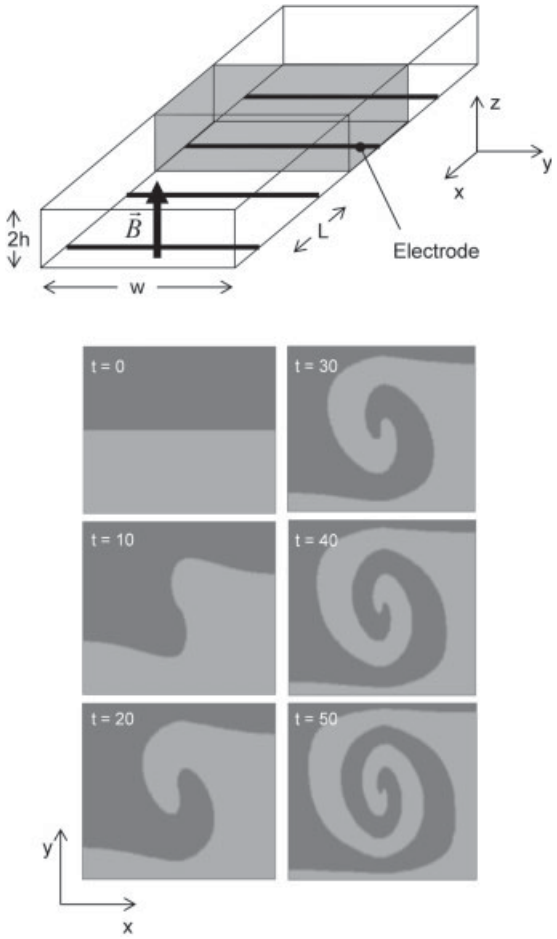

Figure 2.48 The top shows the schematic design of a magneto-hydrodynamic mixer with equally spaced electrodes arranged in a micro channel and an external magnetic field oriented along the *z*-axis. On the bottom theoretical results for the evolution of two parallel liquid lamellae as a function of dimensionless time are shown [146].

Gleeson and West [147] proposed another type of magneto-hydrodynamic micro mixer based on an annular geometry. The device, sketched on the left of Figure 2.49, consists of an annular micro channel, where the curved inner and outer walls of the channel are plated and act as electrodes. Perpendicular to the plane of the channel a magnetic field is applied. Both the electric and the magnetic field are alternating and in-phase. It can be shown that a magneto-hydrodynamic force is induced which acts in the azimuthal direction and drives an azimuthal flow. Gleeson and West obtained a solution of the equations of magneto-hydrodynamics in the form

Figure 2.49 The left side shows the schematic design of an annular magneto-hydrodynamic mixer. On the right, the evolution of the interface between two liquids, as described in [147], is depicted.

of a Fourier–Bessel series. Based on this solution, the growth of the interfacial area of two liquids initially positioned in two 180° azimuthal regions of the mixer was computed. The results of these analyzes are displayed on the right of Figure 2.49. By the azimuthal motion of the fluid, the interfacial area is increased substantially. A calculation of the length of the interface [147] shows that the long-time asymptotics are characterized by a linear increase, a result similar to the findings of Bau et al. [146] for their magneto-hydrodynamic mixer.

Whereas the previous studies were restricted to liquids with dissolved species of zero diffusivity, Gleeson et al. [148] extended their analysis to include finite diffusion constants. They considered the regimes of pure diffusion (zero Peclet number) and intermediate and high Peclet numbers and found analytical and numerical solutions for the mixing time in all three regimes. The predictions derived from the analytical expressions agreed fairly well with the numerical results. It was shown that convection speeds up mixing considerably, for example at Peclet numbers around 10^2 the mixing times are a factor of 10^2–10^3 shorter than the mixing times obtained from pure diffusion.

2.6.7
Hydrodynamic Dispersion

Mass transfer of a solute dissolved in a fluid is not only the fundamental mechanism of mixing processes, it also determines the residence-time distribution in microfluidic systems. As mentioned in Section 1.4, in many applications it is desir-

able to have a narrow residence-time distribution of concentration tracers being transported through a microfluidic system. An initially narrow concentration tracer will suffer a broadening (i.e. a dispersion) due to two different effects. First, in some regions of the flow domain of a system the fluid velocity will be smaller than in others, thus leading to a longer residence time of molecules being transported preferably through these parts of the domain. However, owing to Brownian motion the molecules will also sample some of the other regions with higher flow velocity. Hence molecular diffusion might reduce the dispersion of a concentration tracer. On the other hand, by diffusion an initially localized concentration tracer in a fluid at rest will become dispersed. From these arguments it becomes clear that hydrodynamic dispersion depends on a subtle interplay of convective and diffusive mass transfer, and the evolution of a concentration tracer as it is transported through the flow domain depends on various factors such as the flow profile, and the magnitudes of the flow velocity and the diffusion constant.

The key analysis of hydrodynamic dispersion of a solute flowing through a tube was performed by Taylor [149] and Aris [150]. They assumed a Poiseuille flow profile in a tube of circular cross-section and were able to show that for long enough times the dispersion of a solute is governed by a one-dimensional convection–diffusion equation:

$$\frac{\partial \overline{c}}{\partial t} + \overline{u}\,\frac{\partial \overline{c}}{\partial x} = D_{\mathrm{e}}\,\frac{\partial^2 \overline{c}}{\partial x^2}\,, \tag{103}$$

where $\overline{c}$ denotes the concentration averaged over the cross-section of the tube, $\overline{u}$ the average velocity and D_{e} an effective diffusivity, also denoted dispersion coefficient, which is given by

$$D_{\mathrm{e}} = D + \frac{\overline{u}^2\, R^2}{48\, D}\,, \tag{104}$$

where D is the molecular diffusivity and R the radius of the tube. The factor 1/48 multiplying the velocity-dependent term is generic for tubes of circular cross-section and is modified when other geometries are considered. In many cases the second term, which can be rewritten as $D\,\mathrm{Pe}^2/48$, dominates over the first, which is a purely diffusive contribution. Hence, due to convection a concentration tracer is usually dispersed much more strongly than it would have been by diffusion alone. A notable feature of Eqs. (103) and (104) is their independence of any initial condition. Independent of how the solute is distributed over the channel cross-section and along the channel initially, the description given by Taylor and Aris will be valid in the limit of long times ($t \to \infty$). When exactly this limit is reached with a given accuracy depends on the initialization of the concentration field. A rough guideline is provided by the Fourier number of Eq. (97) evaluated with the tube radius as length scale. The Fourier number can be regarded as a dimensionless time coordinate which compares the actual time with the time a molecule needs to sample the cross-sectional area of the tube. The validity of the Taylor–Aris description should be related to the condition that the Fourier number assumes values of order 1 or larger.

The analysis of Taylor and Aris was extended to arbitrary time values by Gill and Sankarasubramanian [151] for the dispersion of an initially plug-like profile, i.e.

$$c(x,r,0) = \begin{cases} c_0 & (|x| \le l/2) \\ 0 & (|x| > l/2) \end{cases}, \tag{105}$$

where the radial coordinate of the tubular geometry is denoted by r and l is the length of the plug. They derived a generalized evolution equation for the area-averaged concentration of the form:

$$\frac{\partial \overline{c}}{\partial t} = \sum_{n=1}^{\infty} k_n(t) \frac{\partial^n \overline{c}}{\partial x^n} \tag{106}$$

which is valid without any restriction on t. The derivatives in the infinite series appearing on the right side are multiplied by time-dependent dispersion coefficients k_n. In the Taylor–Aris limit, all of the dispersion coefficients except k_1, which describes the convection of the tracer with the flow, and k_2, which determines the spreading of the tracer, are negligible. When moving to smaller times, the time-dependence of k_2 needs to be taken into account, while all higher dispersion coefficients are still negligible [151]. Only at very small times do the higher dispersion coefficients become important. For the case they considered, Gill and Sankarasubramanian found that k_2 can be regarded as time independent for Fourier numbers greater than about 0.5.

Although the results discussed above highlight some of the most important aspects of hydrodynamic dispersion, they were based on cylindrical ducts which are not the generic geometry used in the field of microfluidics. In chemical micro process technology, tubular sections are used to connect different units; however, the channels contained in micro reactors typically have a rectangular or tub-like cross-section. Dispersion in rectangular channels was studied in detail by Doshi et al. [152] and Dutta and Leighton [153]. The evolution equation Eq. (106) is still valid in this case, but the expression for the dispersion coefficient Eq. (104) needs to be modified. While Aris [154] was still able to obtain a simple analytical expression for the dispersion coefficient related to flow between parallel plates, the corresponding expression for rectangular channels is a complicated series expansion. This is not very surprising, since the exact form of the flow profile in a rectangular channel is given in the form of an infinite series as well. Dutta and Leighton [153] found a simple functional dependence which approximates the exact expression for the dispersion coefficient in rectangular channels within an error of 10%. In addition, they considered tub-like channel cross-sections which are typically obtained by isotropic etching processes. For the latter they employed a numerical scheme allowing the computation of the dispersion coefficient. On this basis, they compared different channel geometries and identified favorable and less favorable designs.

While the previous studies refer to straight channels exceptionally, microfluidic devices often comprise channels with a curvature. It is therefore helpful to know how hydrodynamic dispersion is modified in a curved channel geometry. This aspect was investigated by Daskopoulos and Lenhoff [155] for ducts of circular cross-

section. They assumed the diameter of the duct to be small compared with the radius of curvature and solved the convection–diffusion equation for the concentration field numerically. More specifically, a two-dimensional problem defined on the cross-sectional plane of the duct was solved based on a combination of a Fourier series expansion and an expansion in Chebyshev polynomials. The solution is of the general form

$$D_e^{cur} = D\left[1 + Pe^2 f(K,Sc)\right], \tag{107}$$

where D_e^{cur} is the dispersion coefficient in curved ducts, D the molecular diffusivity, Pe the Peclet number of the flow, and the function f depends on the Dean number K defined in Eq. (72) and on the Schmidt number Sc, which is the ratio of the kinematic viscosity and the diffusivity. Daskopoulos and Lenhoff found the following asymptotic behavior for the ratio of the dispersion coefficients in curved and straight ducts:

$$\frac{D_e^{cur}}{D_e} \begin{cases} = 1 & K \to 0 \\ \propto K^{-1} & K \to \infty \end{cases}. \tag{108}$$

As mentioned earlier, in curved channels a secondary flow pattern of two counter-rotating vortices is formed. Similarly to the situation depicted in Figure 2.43, these vortices redistribute fluid volumes in a plane perpendicular to the main flow direction. Such a transversal mass transfer reduces the dispersion, a fact reflected in the K^{-1} dependence in Eq. (108) at large Dean numbers. For small Dean numbers, the secondary flow is negligible, and the dispersion in curved ducts equals the Taylor–Aris dispersion of straight ducts.

Mass transfer in micro channels can exhibit complex dynamics going far beyond the usual dispersion phenomena when adsorption on the channel walls is taken into account. The reason for this complex behavior lies in the kinetics of the adsorption process, which depend on the concentration of the adsporbed species and on temperature [156]. Fedorov and Viskanta [157] set up a model of micro channels with coated walls, where the coating layer adsorbs certain species dissolved in the gas flowing through the channel. They solved the momentum equation in combination with the enthalpy equation and the mass transport equation for the adsorbable species using a finite-difference method. The problem studied was the transport of a step-function concentration and temperature profile through the channel. By virtue of alternating adsorption and desorption processes, complex oscillatory temperature and concentration patterns appeared. Such examples illustrate that when mass transfer dynamics are coupled to adsporption/desorption dynamics at solid surfaces, a behavior qualitatively different from dispersion phenomena in micro channels might emerge.

2.7 Chemical Kinetics

Most plants or reactors in chemical micro process technology inevitably contain a unit where chemical conversion takes place. The goal might be to produce fine chemicals with a high yield and selectivity or to screen a large number of reactions in parallel. Hence a thorough understanding of chemical kinetics is a key requirement for the successful design and optimization of micro reaction devices. For this purpose, reliable models of reaction kinetics coupled to the transport equations of momentum, heat and matter are needed.

2.7.1 Kinetic Models

The effect of chemical kinetics on mass transport in incompressible flows is summarized by the reaction term r in Eq. (89). Applied to a chemical species a, it describes the rate of disappearance of this species per unit volume:

$$r_{\mathrm{a}} = -\frac{1}{V}\frac{\mathrm{d}n_{\mathrm{a}}}{\mathrm{d}t}\,, \tag{109}$$

where n_{a} denotes the molar amount of a. Especially in gas-phase reactions a complicated coupling between chemical kinetics on the one hand and momentum, heat and mass transfer on the other might occur. An exothermic or endothermic reaction releases or consumes energy, an effect which has to be included as a source term in the enthalpy equation Eq. (77). Furthermore, certain chemical species are consumed or produced, which is expressed by the source term in Eq. (89).

The reaction rate r_a determines how fast the concentration of a chemical species a increases or decreases due to chemical reactions. It depends on temperature and on the concentrations of other chemical species involved in the reaction. Consider the case of a simple reaction:

$$\nu_a\, A + \nu_b\, B \rightarrow \nu_c\, C\,, \tag{110}$$

where ν_a, ν_b, ν_c are stoichiometric coefficients and it is assumed that the stoichiometric equation truly represents the mechanism of the reaction. The law of mass action then states that the reaction rate of species a is given by

$$r_a = k\, c_a^{\alpha}\, c_b^{\beta}\,, \tag{111}$$

where k is a rate constant, c_a and c_b denote the species concentrations and $\alpha = \nu_a$, $\beta = \nu_b$. In general, the reaction mechanism will be more complex than suggested by Eq. (110), and the exponents α and β may take non-integer values. The rate constant of many reactions is given by the Arrhenius equation (see, e.g., [126]):

$$k = k_0 \exp\left(\frac{-E}{R\,T}\right), \tag{112}$$

where k_0 is the pre-exponential factor, E the activation energy, R the gas constant and T temperature. The exponential dependence on temperature and the occurrence of an activation energy indicate that the reaction proceeds via an intermediate state which is accessible to the molecules in the high-energy tail of the thermal ensemble.

Power-law kinetic models such as Eq. (111) in combination with the Arrhenius equation and their obvious generalizations to a larger number of reacting species find widespread applications in the simulation of reacting flows. However, strictly the validity of such models is questionable when solid catalytic reactions are considered. Solid catalysis is of major importance in chemical micro process technology, and prominent examples of reactions being conducted in micro reactors are partial oxidations or steam reforming reactions. Such heterogeneously catalyzed reactions are described by more complex models which take into account the adsorption kinetics on the solid surface. In this context, a simple picture of a reaction as described by Eq. (110) could be the following: first, both species are adsorbed to the catalyst surface, where the surface coverage depends on the gas-phase concentration in the vicinity of the surface and on temperature. After having been adsorbed, the species react and the products are released to the gas phase. Assuming first-order adsorption kinetics, the adsorption rate of a chemical species to a catalyst surface can be written as

$$r_{\text{abs}} = F\, s_{\text{abs}} (1 - \theta)\,, \tag{113}$$

where F is the number of molecules per unit area and time hitting the surface, s_{abs} is the adsorption probability at an active site of the surface and θ is the surface coverage, i.e. the percentage of active sites occupied by molecules. The desorption rate is given by

$$r_{\text{des}} = s_{\text{des}}\, \theta\,, \tag{114}$$

with a site-specific desorption probability s_{des}. The adsorption equilibrium is determined by equating the adsorption and the desorption rate. Taking into account that the flux F is proportional to the partial pressure p of the chemical species, the surface coverage can then be written as

$$\theta = \frac{b\, p}{1 + b\, p}\,, \tag{115}$$

where b can be determined from the parameters appearing in Eqs. (113) and (114). Assuming that the species react while being adsorbed at the catalyst surface, the rate of a reaction $A + B \rightarrow C$ is obtained as

$$r = k\, \theta_a\, \theta_b\,, \tag{116}$$

with a rate constant k. The mechanism just described is known as the *Langmuir–Hinshelwood* mechanism and is the most prominent model describing catalysis on solid surfaces. Depending on the specific adsorption and desorption mechanisms, $1 - \theta$ and θ in Eqs. (113) and (114) may have to be replaced by more general ex-

pressions $f_{ads}(\theta)$ and $f_{des}(\theta)$ [156]. Furthermore, the rate equation has to be modified when dissociation reactions have to be taken into account or when an adsorbed species reacts with molecules in the gas phase [126]. For practical applications such as industrial processes it is often very difficult to determine uniquely all the parameters of a Langmuir–Hinshelwood model experimentally. For this reason, often power-law kinetic models such as Eq. (111) are employed to describe solid-catalytic reactions. Such models are usually not justified from a first-principles standpoint, but they may provide a reasonable parametrization of the kinetics in a limited temperature and partial-pressure range.

2.7.2 Numerical Methods for Reacting Flows

Numerical computations of reacting flows are often difficult owing to the different time-scales involved and the highly non-linear dependence of the reaction rate on concentrations and temperature. The solution of the species concentration equations in combination with the momentum and the enthalpy equation generally requires an iterative procedure such as the one outlined in Section 1.3.4. A rough sketch of the numerical structure of a stationary reacting-flow problem is given as

$$\begin{bmatrix} A_{cc} & A_{cu} & A_{cT} \\ A_{uc} & A_{uu} & A_{uT} \\ A_{Tc} & A_{Tu} & A_{TT} \end{bmatrix} \begin{bmatrix} c \\ u \\ T \end{bmatrix} = \begin{bmatrix} b_c \\ b_u \\ b_T \end{bmatrix}, \tag{117}$$

where c, u and T denote the vector of concentration, velocity and temperature fields, respectively. Owing to the non-linear nature of the problem, the coefficients of the different matrices $A_{\alpha\beta}$ still depend on the unknowns c, u and T. The cross-coupling between different field quantities is provided by those matrices $A_{\alpha\beta}$ with $\alpha \neq \beta$. The set of non-linear algebraic equations is solved iteratively, i.e. starting with an initial guess the approximation is successively improved until convergence is reached. Depending on the nature of the chemical reaction term entering the species-concentration equation, different strategies may be applied to solve Eq. (117). For intrinsic kinetics characterized by a much shorter time-scale than transport of momentum, heat and matter, it is often preferable to set up an iteration scheme where a number of iterations of the species-concentration equation are performed during one iteration cycle of the remaining equations. However, for a fast reaction which is heat and mass transfer limited (for example, in a situation where the reactants are not premixed), comparable iteration cycles of the species-concentration equation and the remaining equations might be sufficient.

Apart from the coupling of chemical kinetics with the transport equations, the chemical reaction dynamics itself may pose numerical challenges when a number of different reactions are superposed. In such a case the rate of disappearance of a chemical species i can be written as

$$-\frac{\dot{n}_i}{V} = R_{ij}\, r_j\,, \tag{118}$$

where r_j is the rate of the jth reaction and R_{ij} is a matrix defining how a specific reaction contributes to a change in concentration of the chemical species involved. Frequently it occurs that the time-scales characterizing the different reactions vary by orders of magnitude, such that the fast reactions are already completed while the slow reactions have not yet progressed to any appreciable degree. The corresponding stiff differential equations are usually solved using an implicit time-integration scheme which allows comparatively large time steps without suffering from numerical instabilities or predicting unrealistic asymptotic states [85]. However, implicit time integrators involve the solution of a (generally non-linear) algebraic system of equation for each time step which is done by some iterative scheme such as Newton's method. For reaction systems with a broad spectrum of time-scales, these iteration schemes can fail to converge, with the consequence that very small time steps have to be chosen. Such a situation is related to high computational costs, and methods are needed to simulate extremely stiff reaction systems more efficiently.

Methods based on the partitioning of a reaction system into fast and slow components have been proposed by several authors [158–160]. A key assumption made in this context is the separation of the space of concentration variables into two orthogonal subspaces Q_s and Q_f spanned by the slow and fast reactions. With this assumption the time variation of the species concentrations is given as

$$-\frac{\dot{n}_i}{V} = (Q_{s,j})_i \, (\dot{\gamma}_s)_j + (Q_{f,j})_i \, (\dot{\gamma}_f)_j \, . \tag{119}$$

The notation is such that $(Q_{s,j})_i$, $(Q_{f,j})_i$ denotes the ith component of the jth basis vector in the subspace of slow and fast reactions, respectively. The corresponding expansion coefficients are $(\dot{\gamma}_s)_j$ and $(\dot{\gamma}_f)_j$, respectively, and are expressed by the reaction rates via

$$(\dot{\gamma}_s)_i = \left(Q_{s,j}^T\right)_i R_{jk} \, r_k \, , \tag{120}$$

$$(\dot{\gamma}_f)_i = \left(Q_{f,j}^T\right)_i R_{jk} \, r_k \, . \tag{121}$$

If the time-scale of the fast reactions is much shorter than that of the slow reactions, it can be assumed that the former are completed at an initial stage of the latter. Mathematically, this assumption reads

$$\left(Q_{f,j}^T\right)_i R_{jk} \, r_k = 0 \, . \tag{122}$$

Eq. (122) represents a set of algebraic constraints for the vector of species concentrations expressing the fact that the fast reactions are in equilibrium. The introduction of constraints reduces the number of degrees of freedom of the problem, which now exclusively lie in the subspace of slow reactions. In such a way the fast degrees of freedom have been eliminated, and the problem is now much better suited for numerical solution methods. It has been shown that, depending on the specific problem to be solved, the use of simplified kinetic models allows one to reduce the computational time by two to three orders of magnitude [161].

2.7.3 Reacting Channel Flows

In chemical micro process technology there exists one class of reactor designs which deserves the term 'generic', since many of the micro reactors reported in the literature are based on this design concept. The design comprises at least one rectangular micro channel, often a multitude thereof, with a solid catalyst attached on the channel walls. The reacting fluid flows through the channel, while the reagents diffuse to the channel wall where they undergo chemical reactions. There exist two versions of this design concept, as displayed in Figure 2.50. Either a smooth surface, often a metal layer, acts as catalyst, or the reaction occurs in a catalytically active porous medium. Clearly, the advantage of the porous catalyst layer is the higher specific surface area offering more reaction sites to the reagents. However, all of the studies reported in this section are based on the concept of wall-catalyzed reactions.

For the reasons described above, reaction–convection–diffusion problems tend to be difficult to solve numerically. Hence the simulation of reacting flows in three dimensions or parameter studies of micro reaction devices may be very time consuming. In order to permit rapid prototyping of micro reactors, efficient modeling strategies with a minimum expenditure of computational resources are needed. The modeling approach developed by Gobby et al. [162] allows the assessment of a limited class of reacting micro channel flows very quickly. They assumed a micro channel of length L and depth h with a first-order reaction occurring at one of the channel walls, as depicted in Figure 2.51. In cases where the flow profile is independent of the axial position in the channel and the problem can be approximated by a two-dimensional model, the mass transport equation for a chemical species a can be written in dimensionless form as

$$\frac{\mathrm{Pe}\, h}{L}\, u(\eta)\, \frac{\partial c_a}{\partial \zeta} = \frac{\partial^2 c_a}{\partial \eta^2}\,, \tag{123}$$

where the axial and transverse coordinates ζ and η were non-dimensionalized by the channel length L and the channel depth h. The reactant concentration is denoted by c_a, the velocity by u, and the Peclet number is expressed by the average

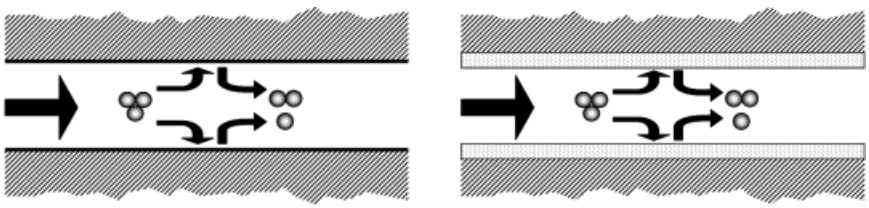

Figure 2.50 Reaction channels with a smooth surface (left) and a porous medium (right) as catalyst.

velocity $\bar{u}$ and the diffusion constant D as $\mathrm{Pe} = \bar{u}\,h/D$. Eq. (123) is solved subject to the boundary conditions of an impermeable upper channel wall and a first-order reaction with rate constant k occurring at the lower channel wall. Such a first-order reaction term surely does not adequately capture the mechanism of heterogeneous catalysis; it might, however, be a reasonable approximation to the kinetics in a limited parameter or operation range. An important dimensionless group characterizing the reactive flow is the Damköhler number, defined as

$$\mathrm{Da} = \frac{k\,h}{D}\,, \tag{124}$$

which characterizes the ratio of the diffusive and the reactive time-scale. The mass transport equation has a separable solution of the form

$$c_a(\zeta,\eta) = \bar{c}_a(\zeta)\,f_a(\eta)\,, \tag{125}$$

where

$$\bar{c}_a(\zeta) = \int_0^1 c_a(\zeta,\eta)\,\mathrm{d}\eta\,. \tag{126}$$

On inserting this ansatz into Eq. (123), the solution can be determined in the form of an eigenfunction expansion, as shown by Walker [163]. The parameter controlling the number of terms of this expansion having to be taken into account is Pe h/L, which is usually of the order of O(0.01 – 1) in micro reactors. For this reason, often only the first term contributes. With the entrance condition $\bar{c}_a(\zeta) = 1$, the axial dependence can then be written as

$$\bar{c}_a(\zeta) = \exp(-\lambda_a\,\zeta)\,, \tag{127}$$

where the eigenvalue λ_a is given as the solution of a non-linear algebraic equation. Gobby et al. compared their analytical results with full numerical simulations and found good agreement. In addition to isothermal flows, they also determined analytical solutions for non-isothermal reacting flows and extended their model to second-order kinetics. Hence they developed a class of models which may provide a simple characterization of reacting flows in micro channels without the need to do a full numerical simulation.

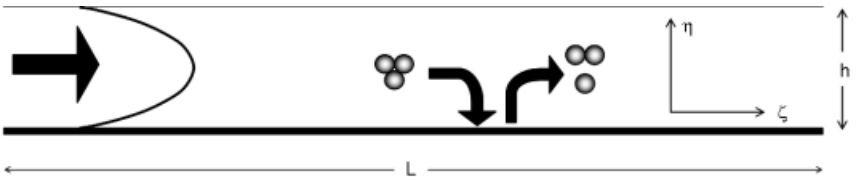

Figure 2.51 Two-dimensional model geometry of a micro channel with a reaction occurring at the lower channel wall.

Commenge et al. [164] used a similar analytical model for reacting flows in micro channels to assess the quality of simple plug-flow models which may be used to estimate reaction-rate constants. Micro reactors lend themselves to measure intrinsic rate constants of chemical reactions, as owing to the short diffusion paths, heat and mass transfer limitations can be eliminated. The simplest way to deduce the rate constant k of a first-order heterogeneously catalyzed reaction at the walls of a tube is by assuming the reaction to occur in the volume of a plug-flow reactor. In this way the wall reaction is replaced by a pseudo-homogeneous reaction and the velocity profile of the flow is ignored, which means that effectively a one-dimensional model is used. By measuring the inlet and outlet concentrations of the reacting component, the rate constant is then obtained as

$$k = \frac{\overline{u}\, R}{2\, L} \ln\left[\frac{c_a(\zeta = 1)}{c_a(\zeta = 0)}\right]. \tag{128}$$

where the notation is chosen similarly to the previous paragraph and L and R measure the length and radius of the tube, respectively. Two effects are not taken into account by this expression. First, radial concentration gradients are ignored. Second, dispersion in the tube, as discussed in Section 2.6.7, is neglected.

Commenge et al. extended the one-dimensional model of reacting flows to include Taylor–Aris dispersion, i.e. they considered an equation of the form

$$\frac{\mathrm{d}^2 c_a}{\mathrm{d}\zeta^2} - \frac{Pe^*}{2}\frac{\mathrm{d}c_a}{\mathrm{d}\zeta} - \beta c_a = 0\,, \tag{129}$$

where Pe^* is a modified Peclet number containing the Taylor–Aris dispersion constant instead of the diffusivity and β is a dimensionless parameter representing the pseudo-homogeneous reaction. In order to study the influence of dispersion on chemical conversion, the solution of Eq. (129) was compared with the solution of the corresponding two-dimensional problem, obtained in a similar way as sketched in the previous paragraph. It turned out that for a Damköhler number of 1, no satisfactory agreement between the one- and the two-dimensional models was achieved. The inclusion of Taylor–Aris dispersion improved the concentration profiles to a certain degree with respect to a plug-flow model; however, the main reason for the deviations are the radial concentration gradients which are not accounted for in the one-dimensional models. Hence, when attempting to extract intrinsic reaction-rate constants from comparisons of experimental results with results of one-dimensional reactor models, care should be taken to work in a regime of Damköhler numbers significantly smaller than 1.

2.7.4 Heat-exchanger Reactors

The design of multichannel micro reactors for gas-phase reactions is typically based on a stack of micro structured platelets. For strongly endothermic or exothermic reactions, it lends itself to alternate between layers of reaction channels and heat-

ing or cooling gas channels which supply energy to or withdraw it from the reaction. Such a set up is similar to the heat exchanger design depicted in Figure 2.30. Within this class of micro reactor designs a choice can be made between different flow schemes of the gas streams in adjacent layers (co-, counter- or cross-current). The counter-current coupling of an endothermic reaction to a heating gas stream in a multi-layer architecture was studied by Hardt et al. [120]. The 2-D geometry their model was based on is displayed in Figure 2.52.

The dynamics of a heterogeneously catalyzed gas-phase reaction occurring in a nanoporous medium in combination with heat and mass transfer was simulated using a finite-volume approach. In contrast to other studies of similar nature, heat and mass transfer in the nanoporous medium were explicitly accounted for by solving volume-averaged transport equations in the porous medium (for a discussion of transport processes in porous media, see Section 1.9). Such an approach made it possible to compare the transport resistances in the gas phase and in the porous medium and to study the trade-off between maximization of catalyst mass and minimization of mass transfer resistance due to pore diffusion. A typical concentration profile of a reacting chemical species which is converted by the catalyst is displayed in Figure 2.53. Owing to the small pore size with an average diameter of 40 nm, the effective diffusivity in the porous medium is small and large concentration gradients build up, whereas in the micro channel the gradients are negligible. Typical catalyst effectiveness factors for a 100 µm catalyst layer were found to be of the order of 0.4. One of the outstanding potential features of micro reactors is an efficient utilization of the catalyst material. In conventional fixed-bed technology, catalyst pellets for liquid reactions are usually of a size of 2–5 mm [126]. Owing to diffusive limitations in such comparatively large pellets, reactions often occur in a region close to the surface.

A main objective of the work of Hardt et al. was to study the influence of heat transfer on the achievable molar flux per unit reactor volume of the product species. They compared unstructured channels to channels containing micro fins such as shown in Figure 2.31. Heat transfer enhancement due to micro fins resulted in a different axial temperature profile with a higher outlet temperature in the reaction gas channel. Owing to this effect and by virtue of the temperature dependence

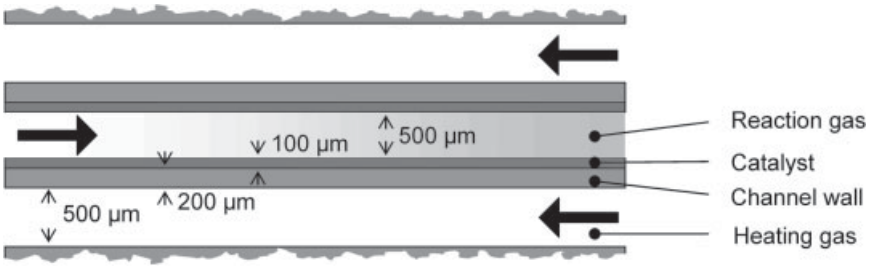

Figure 2.52 2-D model of a counter-current heat-exchanger reactor with a nanoporous catalyst layer deposited on the channel wall.

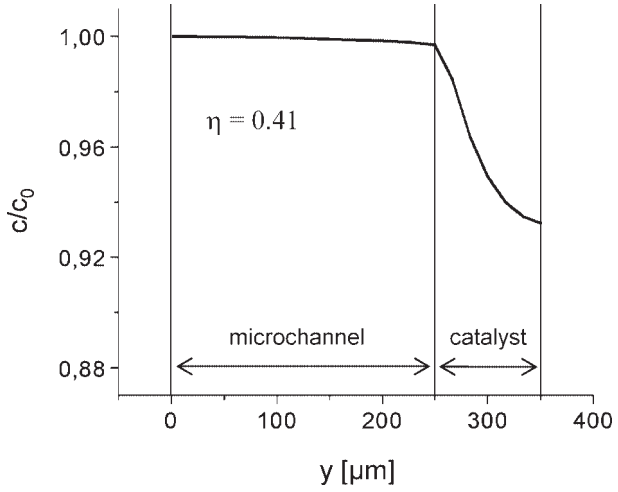

Figure 2.53 Normalized concentration profile of a reacting species across a micro channel of 500 µm width with a 100 µm catalyst layer deposited on the wall.

of the reaction rate, an improvement of heat transfer resulted in a significantly higher specific product molar flux. For the system under study, the heat transfer enhancement achievable with micro fins was found to increase the specific molar flux by about a factor of two. Such model studies show that a complex interplay between flow, heat and mass transfer may occur in micro reactors and underline the need for fully coupled simulations incorporating conjugate heat transfer and transport in porous media.

The optimization of heat transfer in a heat-exchanger reactor was also the objective of the work of TeGrotenhuis et al. [165]. Specifically, the exothermic water–gas shift (WGS) reaction:

$$CO + H_2O \rightleftharpoons H_2 + CO_2 \tag{130}$$

which is utilized in fuel reformers to reduce the level of carbon monoxide was considered. When the temperature level of an exothermic, reversible reaction such as the WGS reaction increases, the kinetics are accelerated but the equilibrium is shifted more towards the feed components. As a result, neither very low nor very high temperatures are optimal when the goal is to maximize the space–time yield for a given conversion. Rather, there is a specific temperature trajectory, i.e. a specific functional dependence of the reaction temperature on time, which allows the space–time yield to be maximized. Owing to their short thermal diffusion paths, micro reactors allow the temperature profile in a reaction channel to be controlled much better than conventional equipment.

TeGrotenhuis et al. studied a counter-current heat-exchanger reactor for the WGS reaction with integrated cooling gas channels for removal of the reaction heat. The computational domain of their 2-D model on the basis of the finite-element method

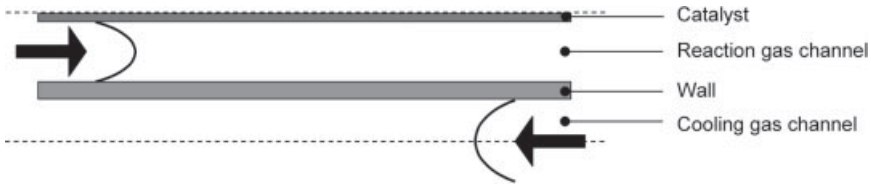

Figure 2.54 Model of a counter-current heat-exchanger reactor for exothermic reactions. The dashed lines indicate symmetry planes.

is sketched in Figure 2.54. The reactor design does not allow for a detailed adjustment of the temperature profile in the reaction gas channel; however, by varying the cooling gas inlet temperature and the ratio of cooling gas and reaction gas flow rates, different temperature profiles can be imposed.

Simulation results for the CO conversion as a function of the ratio of cooling and reaction gas flux are displayed in Figure 2.55. All of the results shown are based on a fixed reaction gas inlet temperature of 350 °C and a fixed inlet composition of the reaction gas. All of the curves obtained with different cooling gas inlet temperatures start at a conversion of about 70%. This is due to the fact that by release of reaction heat close to the inlet, the reaction gas temperature rises to above 400 °C, a region where the conversion is limited to 70% by the chemical equilibrium. The maximum achievable conversion increases by 2.7% when the cooling gas temperature is raised from 125 to 225 °C. The reaction dynamics are such that, owing to the fast kinetics at high temperatures, a large degree of conversion is obtained in the inlet region of the channel. For the remaining few percent conversion, a comparatively large reactor volume is needed. Hence even minor differences in conversion

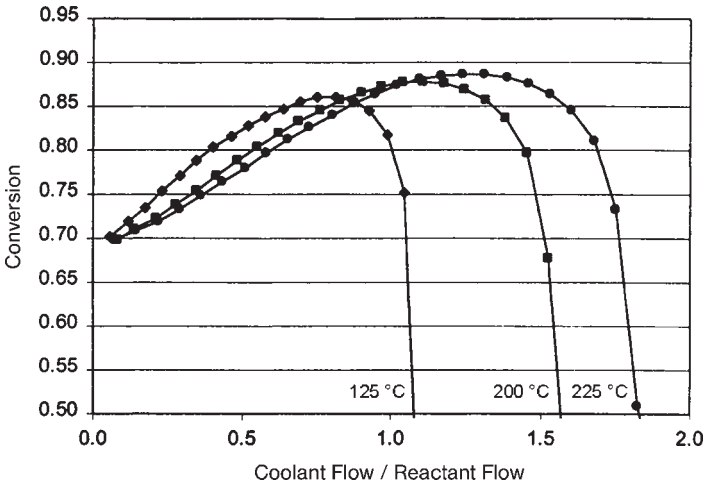

Figure 2.55 The effect of cooling gas flow rate and inlet temperature on CO conversion in the WGS reactor, as described in [165]. The cooling gas flow rate was varied for a fixed reaction gas flow rate and three different inlet temperatures were considered.

achievable with improved temperature control may result in a considerable reduction in reactor size and the required amount of catalyst. When considering more advanced reactor designs allowing for fine-tuning of the temperature trajectory, CFD simulations are indispensable for performance optimization.

2.7.5 Periodic Processing

As compared with macroscopic reactors, micro reactors not only permit fast heat and mass transfer, they also allow improved process control. In this context, one aspect that has been studied in some detail is periodic process control. It is well known that in some cases periodic variations of the process parameters permit improved reactor performance [166–168]. In macroscopic reactors, short cycle times are often not accessible owing to limitations of heat and mass transfer. In micro reactors, the large heat transfer coefficients achievable allow rapid thermal cycling. Furthermore, low-Peclet number flow in narrow channels allows concentration plugs to be transported without axial mixing. The potential of periodic process control for enzymatic reactions in micro reactors was investigated by Stepanek et al. [169]. They studied a reaction–adsorption process in a micro channel with alternating wall segments, as displayed on top of Figure 2.56. The channel comprises alternating segments with reaction and adsorption zones. In the reaction zones an

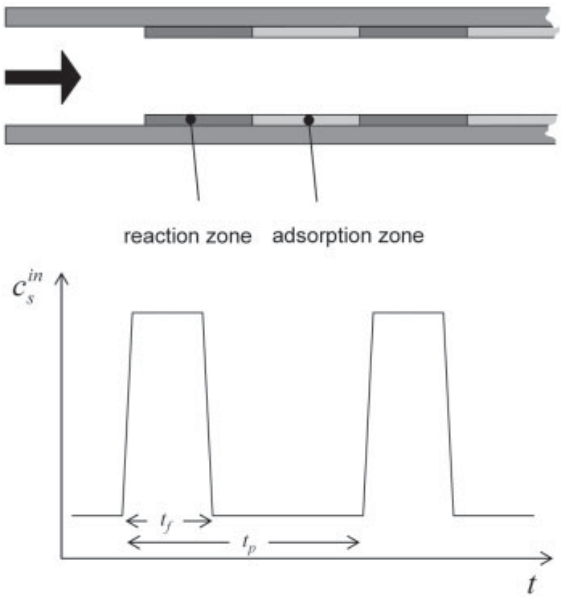

Figure 2.56 Micro channel with alternating segments for reaction and adsorption (above) and operating cycle with pulsed substrate inlet concentration (below).

immobilized enzyme catalyzes the synthesis of a biomolecule, which can be removed from the flow by wall adsorption in the adsorption zones. The reason for such different channel segments is the kinetics of the reaction which show both product and substrate inhibition, i.e. the reaction rate decreases with increasing substrate and product concentration. Hence, by removing the product from the flow in the adsorption zones, the reaction rate can be increased.

Stepanek et al. [169] used a one-dimensional plug flow model to describe the reaction dynamics in a micro channel for a periodic processing regime. In such a model the reaction is regarded as pseudo-homogeneous. An additional reaction term was included for the product to describe removal from the flow by adsorption. The partial differential equations for the two chemical species, substrate and product, were solved for periodic inlet conditions which are depicted on the bottom of Figure 2.56. For a fraction t_f/t_p of the temporal period t_p, the substrate concentration at the inlet is adjusted to a specific value and the pH is chosen in such a way as to promote product adsorption. For the remaining fraction of the period, the substrate concentration is zero and the pH is shifted to values favoring elution.

Typical results for the outlet concentration of substrate and product are shown in Figure 2.57 for two different values of t_f/t_p. When $t_f/t_p = 0.9$, for most of a cycle the

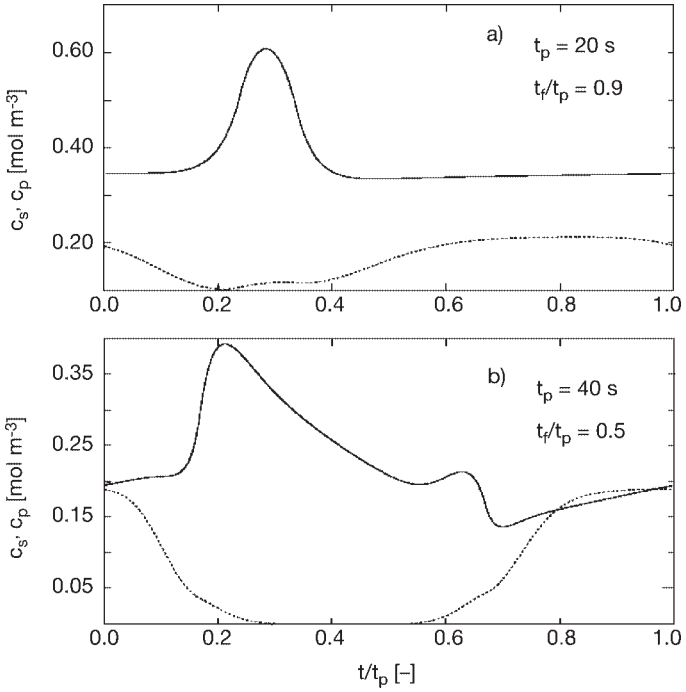

Figure 2.57 Substrate (dashed line) and product (full line) concentrations at the channel outlet for two different operation modes, taken from Stepanek et al. [169].

substrate is fed to the channel, whereas the substrate inlet concentration is zero for half of the cycle when $t_f/t_p = 0.5$. In the former case, the average product concentration is fairly high, but substrate and product are not easily separated, since for most of the cycle a mixture of substrate and product is found at the channel outlet. In the latter case, the average product concentration is lower, but the separability of substrate and product is considerably higher. Stepanek et al. [169] made a systematic parameter study of the reactor varying the cycle period, the switch-on time of the substrate and the inlet flow velocity. They found a trade-off between product yield and separability of the different chemical components. A high product yield usually resulted in a mixture of product and substrate (low separability) at the outlet and vice versa. Furthermore, the reactor performance increased with decreasing cycle time. Hence, in cases where the capital and/or the process costs for product separation are considerable, a micro reactor with periodic process control may offer a solution, since an adjustment of the process parameters allows a product separation *in situ* and the reactor can be operated with favorable short cycle times.

2.8 Free Surface Flow

Multi-phase flows of immiscible fluids are omnipresent in chemical process technology. In various processes, gases or liquids are dispersed in a surrounding liquid phase, or aerosols of liquid droplets in a gas phase are formed. A standard method to model such types of flow is the Euler–Euler description of interpenetrating continua [171]. In this approach, both the disperse phase, i.e. the droplets or the bubbles, and the surrounding continuous phase are treated as continua which occupy a certain fraction of each volume element of the fluid domain. Via exchange terms in the transport equations, the two phases are coupled to each other and may exchange momentum, heat and matter. In micro reactors the Euler–Euler description is often inappropriate. When the size of droplets or bubbles becomes comparable to the channel dimensions, the continuum assumption breaks down and the dynamics of multi-phase flow confined in narrow spaces deviates considerably from that in macroscopic vessels. Hence, in general the usual modeling approaches for multi-phase flow cannot be applied in micro reactors and special techniques are needed to predict the flow patterns.

In most cases the only appropriate approach to model multi-phase flows in micro reactors is to compute explicitly the time evolution of the gas/liquid or liquid/liquid interface. For the motion of, e.g., a gas bubble in a surrounding liquid, this means that the position of the interface has to be determined as a function of time, including such effects as oscillations of the bubble. The corresponding transport phenomena are known as *free surface flow* and various numerical techniques for the computation of such flows have been developed in the past decades. Free surface flow simulations are computationally challenging and require special solution techniques which go beyond the standard CFD approaches discussed in Section 2.3. For this reason, the most common of these techniques will be briefly introduced in

this section, followed by a number of examples highlighting their application in the field of micro process technology.

2.8.1 Computational Modeling of Free Surface Flows

In order to describe correctly the dynamic evolution of a fluid/fluid interface, a number of boundary conditions have to be implemented into the computational models.

The kinematic condition requires that no fluid can transverse the interface, i.e. the local flow velocity u_i relative to the velocity of the interface u_i^{int} should be zero

$$(u_i - u_i^{\mathrm{int}})\, n_i\big|_{\mathrm{int}} = 0\,, \tag{131}$$

where n_i are the components of a unit vector normal to the interface and the whole expression is to be evaluated at an interfacial position.

The dynamic condition requires that the net force on any portion of the interface has to vanish. In a local coordinate frame attached to an interfacial position, three constraints are derived expressing the force balance for each of the three coordinate directions:

$$n_i\, \tau_{ij}\, n_j\Big|_1 + \sigma\left(\frac{1}{R_t} + \frac{1}{R_s}\right) = -n_i\, \tau_{ij}\, n_j\Big|_2\,, \tag{132}$$

$$n_i\, \tau_{ij}\, t_j\Big|_1 - \frac{\partial \sigma}{\partial t} = n_i\, \tau_{ij}\, t_j\Big|_2\,, \tag{133}$$

$$n_i\, \tau_{ij}\, s_j\Big|_1 - \frac{\partial \sigma}{\partial s} = n_i\, \tau_{ij}\, s_j\Big|_2\,, \tag{134}$$

where τ_{ij} represents the stress tensor, σ the interfacial tension and R_t and R_s, the radii of curvature of the interface along the two orthogonal coordinate directions. The subscripts 1 and 2 refer to the two different phases. The position vector is expressed by two unit vectors t_i and s_i in the tangent plane of the interface and one orthogonal unit vector n_i as

$$\mathbf{r} = t \cdot \mathbf{t} + s \cdot \mathbf{s} + n \cdot \mathbf{n}\,. \tag{135}$$

Eq. (132) states that the interfacial tension has to be balanced by a pressure difference between the two phases. The terms containing derivatives of σ in Eqs. (133) and (134) are non-zero only if there are local variations of the interfacial tension, which might be due to differences in concentration or temperature. The flow induced by such an effect is known as Marangoni convection.

The constraint to be implemented at the three-phase contact line between the two fluids and a solid surface requires that the contact angle θ (compare Figure 2.58) assumes a prescribed value. As discussed in Section 2.2.3, the contact angle might also be allowed to vary with the velocity of the contact line. Especially in microfluidic

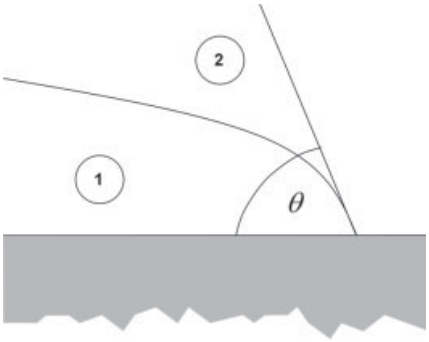

Figure 2.58 Two fluids in contact with a solid surface at a contact angle θ.

systems surface effects often dominate over volumetric effects. Therefore, a correct implementation of the boundary conditions outlined above is of major importance for the modeling of free surface flows in micro reactors.

There are two major classes of numerical methods for free surface flow simulations, *interface tracking* and *interface capturing* methods. In the interface tracking method (see, e.g., [172] or [173]), the interface coincides with a specific grid line, i.e. each cell either belongs to phase 1 or phase 2. When the interface becomes deformed, the grid follows its motion and the grid cells are adjusted in such a way that their identification with the fluid phases is maintained. An example of a corresponding grid deformation for a gas/liquid free surface flow is shown in Figure 2.59. In that case, only the liquid is modeled, and the stresses exerted on the surface by the gas phase above the liquid are so small that they can be neglected. The part of the grid shown in the figure follows the motion of a surface wave travelling from right to left. An advantage of the interface tracking method is the fact that by construction a sharp, well-localized interface is maintained throughout the simulation. Furthermore, in the case of gas/liquid flows the gas can often be neglected and only the liquid domain needs to be modeled, as indicated in Figure 2.59. However, a disadvantage is the fact that changes in topology of the flow domain, for example the decay of a liquid volume into droplets or droplet coalescence, are difficult to take into account. As such processes play an important role in chemical process technology, interface tracking methods will not be further considered here.

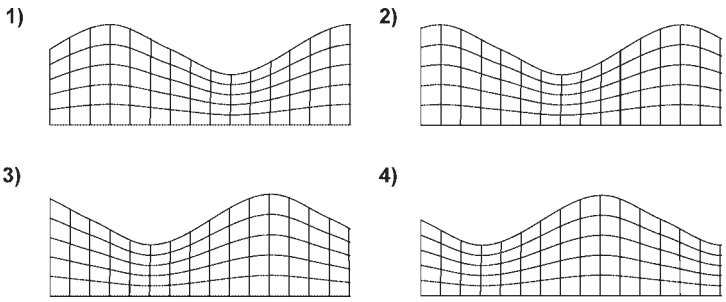

Figure 2.59 Grid deformation following a wave propagating from right to left on a liquid surface.

In contrast to the interface tracking method, in interface capturing techniques a fixed grid is used. Relative to that grid the two fluid phases move and the location of the interface has to be reconstructed. In general, different fluid phases cannot be uniquely assigned to different cells, there may be cells containing fractions of both fluids. The great advantage of interface capturing methods lies in their ability to model in principle all kinds of topological changes fluid volumes surrounded by a second immiscible phase might undergo. A disadvantage of some interface capturing methods is an artificial smearing of the interface due to numerical diffusion, as discussed in Section 2.3.1. Furthermore, local or even global mass conservation is sometimes not guaranteed, and the grid always needs to be larger than the fluid volume to be considered, since it is not co-moving with the fluid.

Among interface capturing methods, one of the most popular and most successful schemes is the volume-of-fluid (VOF) method dating back to the work of Hirt and Nichols [174]. The VOF method is based on a volume-fraction field c, assuming values between 0 and 1. A value of $c = 1$ indicates cells that are filled with phase 1, and phase 2 corresponds to $c = 0$. Intermediate values of c indicate the position of the interface between the phases; however, the goal is to maintain a sharp interface in order to identify the different fluid phases uniquely. Volumes assigned to the different phases are moving with the local flow velocity u_i, and therefore the evolution of c is determined by a convection equation:

$$\frac{\partial c}{\partial t} + \frac{\partial}{\partial x_i}(u_i\, c) = 0\,. \tag{136}$$

Via Eq. (136) the kinematic condition Eq. (131) is fulfilled automatically. Furthermore, a conservative discretization of the transport equation such as achieved with the FVM method guarantees local mass conservation for the two phases separately. With a description based on the volume fraction function, the two fluids can be regarded as a single fluid with spatially varying density and viscosity, according to

$$\rho = \rho_1\, c + \rho_2\,(1 - c), \quad \mu = \mu_1\, c + \mu_2\,(1 - c)\,, \tag{137}$$

where the subscripts 1 and 2 refer to phase 1 and 2, respectively.

When the transport equation for c is solved with a discretization scheme such as upwind, artificial diffusive fluxes are induced, effecting a smearing of the interface. When these diffusive fluxes are significant on the time-scale of the simulation, the information on the location of different fluid volumes is lost. The use of higher order discretization schemes is usually not sufficient to reduce the artificial smearing of the interface to a tolerable level. Hence special methods are used to guarantee that a physically reasonable distribution of the volume fraction field is maintained.

A simple method used to maintain a sharp interface is based on a correction algorithm [175]. After each time step, the amount of fluid of a specific phase having penetrated the interface at $c = 0.5$ is determined. Then the fluid is redistributed such that the 'voids' on the other side of the interface are filled up. The redistribution is done globally, as information on the origin of fluid volumes having pen-

etrated the interface is not available. Owing to the global nature of the correction step, mass conservation is only fulfilled globally and not locally. Especially when a number of disconnected fluid volumes exist (for example, various droplets), artefacts might be induced by the correction algorithm. The artefacts show up as an exchange of mass between the disconnected volumes, i.e. one volume might increase at the expense of another.

Typically, the interface obtained with the versions of the VOF method described above is smeared over a few grid cells, which, on sufficiently fine grids, allows one to identify uniquely the simply connected volumes belonging to the different phases. Instead of regarding the dynamic conditions of Eqs. (132)–(134) as boundary conditions, surface tension can be implemented as a volume force in those cells where c lies between 0 and 1. In the method developed by Brackbill et al. [176], a momentum source term of the form

$$(f_{\mathrm{st}})_i\,(x_j) = \sigma\,\kappa(x_j)\,\frac{\partial c(x_j)}{\partial x_i} \tag{138}$$

is added to the Navier–Stokes equation, where σ is the interfacial tension and κ the local curvature of the interface. Owing to the spatial derivative appearing in Eq. (138), the interfacial tension acts only in those regions where steep gradients of the volume-fraction field exist, which are the regions around the interface. Even for a sharp interface, the description given by Brackbill et al. can still be applied when c is replaced by a smoothed volume-fraction function $\tilde{c}$, which is the result of the convolution of c with, e.g., a Gaussian kernel.

In the methods described above, *a priori* no information on the position of the interface within computational cells or on the radii of curvature of the interface is available. This information has to be obtained from the values of the volume-fraction field in the neighborhood of the point of interest. However, in some versions of the VOF method, an algorithm allowing tracking the position of the interface within single computational cells is available. Two important examples of such algorithms are the Single-Line Interface Construction (SLIC) [177] and the Piecewise-Linear Interface Construction (PLIC) (see [178] and references therein) schemes. In the SLIC scheme for rectangular grids the interface in each computational cell is represented as a line (or a plane in 3-D) which is parallel to the faces of the cell. The more exact PLIC scheme still assumes a linear interface within single computational cells, but allows for an arbitrary interface orientation. A basic form of the SLIC algorithm is represented graphically in Figure 2.60. The interface orientation within a cell in a specific time step depends on the status of the cell under consideration and its neighbors in the previous time step. The figure shows an 'upwind' cell and a cell located downstream with respect to the local flow velocity (the 'downwind' cell). Depending on the status of both of these cells, the interface orientation in the next time step is computed according to the diagram on the right. In this context, a cell shaded in gray contains fluid 1 (for example, a liquid), a white cell fluid 2 (for example a gas) and a hatched area represents a cell containing a mixture of both fluids.

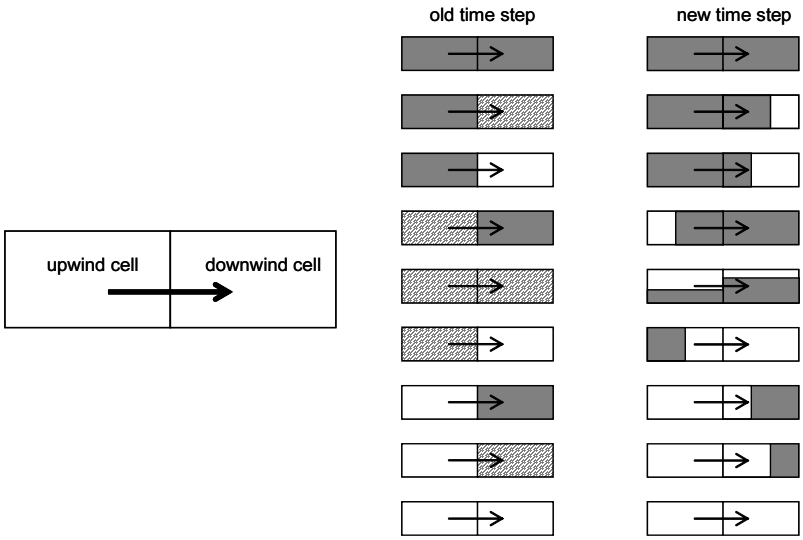

Figure 2.60 Pictorial representation of the SLIC scheme showing the updating scheme for an upwind and a downwind cell. Cells filled with fluid 1 are indicated in gray, those with fluid 2 in white. Cells containing a mixture of both fluids are represented by hatched areas. In the right column the configuration at the new time step is shown, with interface positions depicted explicitly.

Within the PLIC scheme, an interface is allowed locally to stand at any tilted angle with respect to the grid cell. Such a more realistic description goes along with increased accuracy and computational complexity. By reconstructing the position of the interface within single computational cells, both the SLIC and PLIC schemes add information on sub-grid scales to the VOF model. In such a way, a sharp interface is maintained throughout the complete simulation and volumes belonging to different immiscible fluids may be tracked accurately over long time-scales.

Another popular class of schemes for interface capturing is constituted by level-set methods, introduced by Osher and Sethian [179]. Level-set methods are based on the same type of equation as Eq. (136), but the field c is no longer interpreted as a volume fraction field. Instead, c is regarded as a level-set function, assuming positive values in the regions occupied by fluid 1 and negative values in the regions of fluid 2. The interface is interpreted as the surface for which c is equal to zero. The absolute values of c measure the distance to the interface, which, by construction, is always maintained as a well-defined surface, since it is simply identified with the value $c = 0$. However, the price to pay for this somewhat artificial construction is a violation of mass conservation. In order to enforce mass conservation, algorithms have been developed which re-initialize c after a number of time steps based on a special evolution equation [180].

In addition to the methods described above, there exist a number of other methods for the computation of free-surface flows which allow a sharp interface to be maintained. The approach which resembles computational methods for single-

phase flows most closely is the front-tracking scheme. This technique essentially assumes a single fluid with local variations of density and viscosity, thus allowing modeling of different phases. The interface is marked by tracer particles moving with the local flow velocity. Surface tension is included as a volumetric force being applied to the computational cells in the vicinity of the interface.

A current version of the front-tracking method was developed by Tryggvason et al. [181]. As the tracer point density may become too small or too large in specific regions during the evolution of the interface, their algorithm creates additional points or deletes points wherever necessary. For 3-D problems, the tracer points are connected by triangular elements which may then have to be subdivided or merged. Since the front is represented by a line or a surface over which the points are distributed, a scheme for smoothing the surface tension on to the higher dimensional computational grid is needed. The advancement of the tracer particles is done with the local flow velocity, thus ensuring that there is no flow across the interface. Changes in the front topology are difficult to model in the framework of front-tracking schemes. Essentially it is necessary to equip the method with a search algorithm which determines interfacial sections that are close to each other and decides to change the connectivity of the interface whenever needed.

2.8.2 Micro Flows of Droplets and Bubbles

Owing to the transient nature of free-surface flows, the simulation of corresponding flow phenomena in multi-phase micro reactors remains a challenge, especially when 3-D models are needed. Nevertheless, in a few examples the use of surface capturing methods to study free-surface flows for applications in micro process technology has been demonstrated. So far the work has been focused mostly on pure flow phenomena and seems to have been restricted to non-reacting flows. One of the best established applications of micro process technology in the context of multi-phase flows is the generation of emulsions and dispersions. Although micro mixers showed some advantages for creating disperse systems compared with, e.g., conventional stirred tanks, it remained unclear by which physical mechanism droplet or bubble formation occurs and how the formation mechanism can be varied and regulated to create tailor-made emulsions and dispersions. In order to understand the physical phenomena better, multilamination mixers were fabricated from glass, thus allowing optical images to be taken showing the formation of droplets or bubbles. In parallel, simulations based on the VOF method were carried out, the results of which have been summarized [182, 183]. As an example of the experimental results, the formation of water droplets in silicone oil in a multilamination mixer with a rectangular mixing chamber is shown in Figure 2.61. From the figure it is apparent that in the mixing chamber liquid 'lamellae' are formed which subsequently decay into droplets.

The decay of liquid lamellae of circular cross-section at rest was studied in a 2-D model using the VOF method without subcellular tracking of the interface (in the following denoted 'basic VOF method') in combination with a correction algorithm

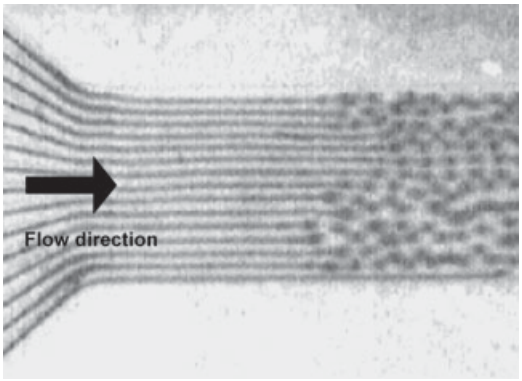

Figure 2.61 Formation of water droplets in silicone oil in a multilamination micro mixer.

to compensate numerical diffusion [175]. In order to initiate the decay, a sinusoidal fluctuation was imposed on the surface of the cylinder. The corresponding time evolution of a water cylinder is shown in Figure 2.62. The initial fluctuation imposed on the surface becomes damped, but initiates a decay of the cylinder into droplets with about twice the wavelength of the initial perturbation. The CFD results are in agreement with linear hydrodynamic stability theory pioneered by Rayleigh (see, e.g., [184]). Rayleigh stability theory predicts that fluctuation wavelengths below a certain cut-off are damped, and that a liquid cylinder decays with a

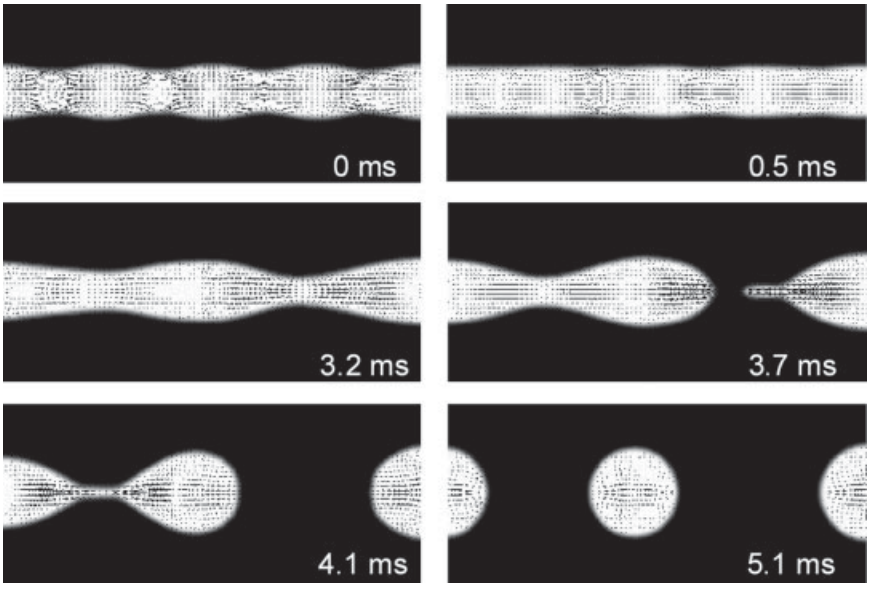

Figure 2.62 VOF-based simulation of a water cylinder decaying into droplets by a hydrodynamic instability [182].

preferred wavelength. In the free-surface flow simulation the correct decay wavelength is selected [182].

While the 2-D simulation has to be regarded as a test case rather than a serious attempt to describe droplet formation in micro mixers, a more elaborate 3-D model incorporating the actual geometry of the mixing chamber and a non-zero flow velocity was set up, again using the basic VOF method. Specifically, the system silicone oil/water was considered at various flow rates. Also with the 3-D model liquid lamellae were found to decay into droplets, while the decay mechanism depends on the contact angle between the glass surface and the two fluids. At contact angles of about 40° (referring to a drop of silicone oil resting on a glass surface and surrounded by water), almost cylindrical rods of water detaching from the walls of the mixing chamber are formed; at contact angles close to 90° the liquid lamellae of approximately rectangular cross-section are still in contact with the channel walls when they decay into droplets [183]. Snapshots of these two different droplet formation mechanisms are shown in Figure 2.63.

Experimentally, contact angles around 40° were determined for the system under study, which means that droplet formation should proceed as shown on the left of Figure 2.63. For a quantitative comparison of experiments and simulations, the droplet diameter, the decay wavelength (i.e. the distance between successive droplets) and the diameter of the water lamellae were determined [183]. In general, the agreement between the simulation results and the experimental data was fairly good. Especially the decay wavelength was found to agree reasonably with Rayleigh's linear stability theory, thus indicating that droplet formation occurs through the well-known Rayleigh plateau instability. Obviously, the dynamics of droplet formation are influenced by shear forces due to the non-zero flow velocity inside the mixer only to a very small extent. Based on this work, it may be claimed that one significant dynamic aspect of emulsion formation in micro mixers was revealed.

Another numerical study of free-surface flow patterns in narrow channels was conducted by Yang et al. [185]. They considered the flow of bubbles of different size driven by body forces, for example the rising of bubbles in a narrow capillary due to buoyancy. The lattice Boltzmann method [186] was used as a numerical scheme

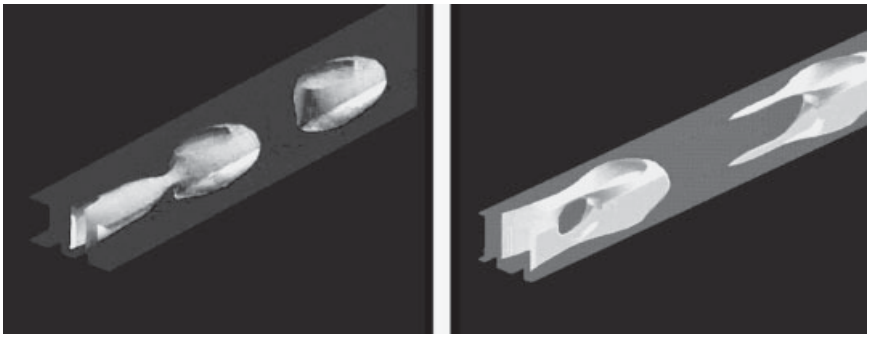

Figure 2.63 Droplet formation in a micro mixer for a wall contact angle of 40° (left) and 90° (right), with silicone oil being the continuous and water the disperse phase.

which recovers a numerical solution of the Navier–Stokes equation from a solution of the Boltzmann equation. Correspondingly, in addition to the computational grid in position space, a grid in velocity space is introduced and a collision term is used which rapidly drives the phase-space distribution into thermal equilibrium.

An important quantity determining the nature of the bubble flow considered by Yang et al. is surface tension, which often plays a dominant role in free-surface micro flows. However, viscous forces are also important in many cases. Hence the ratio of the viscous force and the surface tension force:

$$\mathrm{Ca} = \frac{\mu u}{\sigma} \tag{139}$$

termed 'capillary number', is an important dimensionless group characterizing the flow. When a bubble of diameter d enters a capillary of smaller diameter, a thin liquid film is formed between the bubble and the capillary wall. A quantity which has been determined experimentally is the thickness of this liquid film. Yang et al. compared their simulation results with corresponding experimental results for a range of capillary numbers between 0 and 0.117 and found good agreement. An interesting result of their studies is the fact that the rise velocity depends strongly on the bubble size. Owing to this effect, coalescence occurs in a rising column of bubbles of different sizes. The evolution of such a multi-bubble arrangement is shown in Figure 2.64. The smaller bubbles approach the bigger ones in front of them and undergo coalescence. For an ensemble with a certain size distribution this is a multi-step process, as shown in the figure.

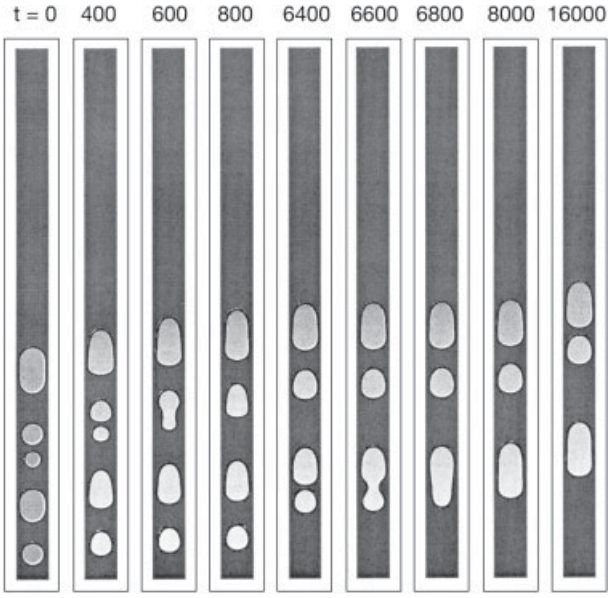

Figure 2.64 Time sequence showing the movement and coalescence of an ensemble of bubbles in a narrow capillary, taken from [185].

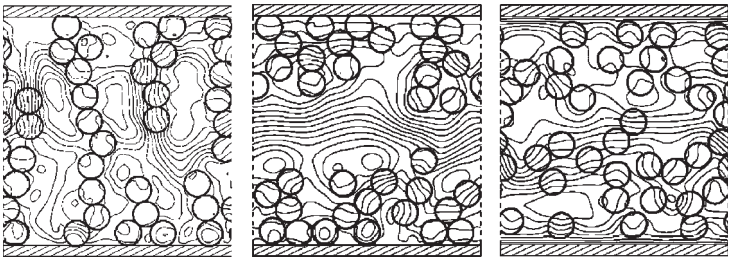

Figure 2.65 Droplet distribution in a channel due to an electric field perpendicular to the channel walls, as described in [187]. At vanishing flow rate the droplets line up in columns (left) and accumulate at the walls as the flow rate is increased (middle). At comparatively high flow rates the droplets get resuspended over the channel (right).

In another study of free-surface flow in confined geometries, Tryggvason et al. [187] used their front-tracking method to study the movement of droplets in channels under the influence of an electric field. When droplets are suspended in a phase of different conductivity and dielectric permittivity, the dielectric mismatch between the two phases induces a stress at the fluid interface. Furthermore, in an external electric field the droplets attain a dipole moment. The dipoles attract each other and the droplets tend to line up in columns. Tryggvason et al. studied the conformation of a droplet suspension in a channel limited by two parallel plates between which an electric field is applied. At vanishing flow rate the droplets line up in columns between the plates, as depicted on the left of Figure 2.65. The lines in the figure represent the streamlines of the flow. When the flow is turned on, the columns break up and the droplets accumulate at the walls. At comparatively high flow rates, the droplets are resuspended all over the channel, as shown on the right of Figure 2.65. Although giving valuable insight into the dynamics of, e.g., micro emulsions inside electric fields, these simulations still suffer from the fact that droplet coalescence has not been accounted for.

2.9 Transport in Porous Media

In the last few years, an increasing number of micro reactors containing micro channels with porous catalyst layers have been reported [13, 14]. In addition to such devices providing a large specific surface area, also the smooth metal surface of the channel walls itself was used as catalyst. The latter approach is suited for proof-of-principle studies rather than the development of systems meeting certain performance requirements such as a specific molar flux of the desired product. Nowadays, micro reactors are starting to be utilized in commercial processes. Hence demands for reaching certain performance benchmarks are raised and the use of smooth metal surfaces as catalysts often is no longer sufficient owing to the disadvantageous surface-to-volume ratio as compared with porous catalyst media.

Porous media have a long-standing history in chemical process technology. One important application is the use of fixed beds of catalyst pellets for heterogeneously catalyzed gas-phase reactions, where a gas mixture is being chemically converted in a tubular section filled with catalyst. In such processes gas is forced through the voids between the pellets by a pressure gradient and the mass transfer characteristics are determined by the transport of chemical species from the void space to the pellet surface and by diffusion within the porous pellets themselves. Analogously, porous media find their application as catalyst carriers in micro reactors. However, in contrast to the fixed-bed technology, porous layers are attached to the micro channel walls with a gas flow passing by.

Owing to the importance of transport in porous media not only in chemical process technology but also in other areas such as geology, more than a century of intense research has resulted in a variety of theoretical and experimental results. Depending on whether flow, heat or mass transfer is considered, a number of different transport mechanisms have to be taken into account. Flow through a porous medium is equivalent to convection of a fluid through the voids or the pore throats. Mass transfer is often dominated by diffusive transport and, similar to flow, occurs exceptionally in the void space of the porous medium. In contrast, heat transfer may occur in the fluid occupying the voids and also in the surrounding solid phase. In chemical micro process technology with porous catalyst layers attached to the channel walls, convection through the porous medium can often be neglected. When the reactor geometry allows the flow to bypass the porous medium it will follow the path of smaller hydrodynamic resistance and will not penetrate the pore space. Thus, in micro reactors with channels coated with a catalyst medium, the flow velocity inside the medium is usually zero and heat and mass transfer occur by diffusion alone.

2.9.1 Morphology of Porous Media

A porous medium consists of a pore space and a solid matrix. Depending on the chemical composition and the preparation technique used to deposit the porous catalyst layer on the micro channel walls, a variety of pore space geometries and topologies may be found. Figure 2.66 shows an image of a catalyst layer deposited in a micro channel using a wash-coat technique and a scanning electron microscopy (SEM) image of the surface morphology of such catalyst carriers. The SEM image gives an impression of the pore structure of the catalyst layer. One of the most important quantities characterizing a porous medium is the porosity ε, defined as the volume fraction of the pore space. The porosity of some materials, e.g. foams, may assume values in the proximity of 1 [117]. An important topological feature of a porous medium is the coordination number Z, defining the number of pore throats meeting at a node of the pore space. Another essential topological aspect is the existence of closed loops in the pore network, i.e. alternative pathways connecting two given points. On a larger scale, the connectivity of the pore space is an aspect which influences the transport properties of the medium. For a given mate-

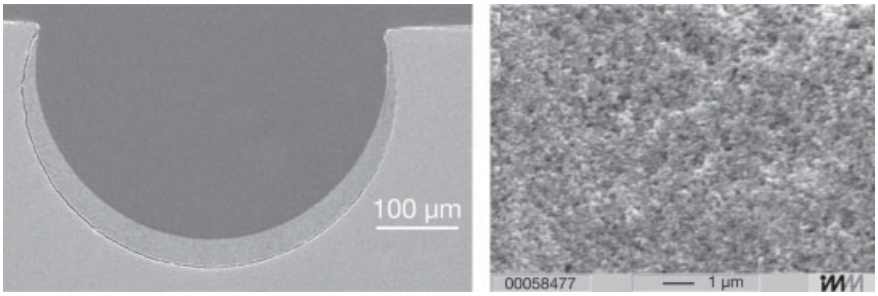

Figure 2.66 Cross-section of a micro channel coated with a catalyst layer (left) (source: INM, Saarbrücken, Germany) and typical surface morphology of wash-coat catalyst carriers (right).

rial sample there might not exist a sample-spanning cluster of pores connecting two opposite boundaries. In such a case, flow or mass transfer between these boundaries cannot occur. Besides these topological features, the geometry of the pore space characterizes a porous medium. Roughly speaking, there might be comparatively small nodes connected by long pore throats, or there might exist a pore space which is dominated by the nodes and does not possess distinct pore throats.

2.9.2 Volume-averaged Transport Equations

As far as modeling of transport phenomena in porous media is concerned, the task is to provide a generic description which is applicable to as broad a class of materials as possible. The models should to some extent be idealized, allowing them to capture a broad class of phenomena without the need to model all geometric details of the pore space and allowing for a fundamental understanding of transport processes in porous media.

A popular semi-empirical approach is to assign effective transport coefficients to the porous medium. In the context of such models, taking heat transfer as an example, the porous medium would act as if it was equipped with an effective thermal conductivity λ_e being a function of the fluid and solid thermal conductivity λ_f and λ_s. The formal justification of this approach relies on a volume-averaging procedure for the local transport equations. In Figure 2.67 a schematic representation of a porous medium together with the volume over which the averaging is performed is displayed. The averaging volume should be much larger than a typical pore dimension and much smaller than the size of the material sample taken into consideration in order to allow for meaningful variations of the field quantity being looked at. In the case of heat conduction in a porous medium, the fundamental equation to be solved is

$$(\rho\, c_p)_i \frac{\partial T_i}{\partial t} = \frac{\partial}{\partial x_k}\left(\lambda_i \frac{\partial}{\partial x_k} T_i\right), \tag{140}$$

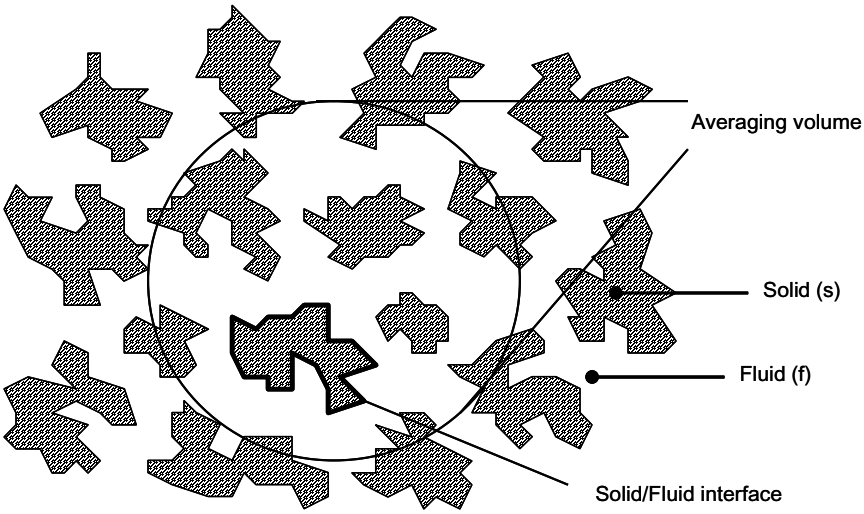

Figure 2.67 Microstructure of a porous medium together with sample volume over which field quantities are averaged.

where ρ, c_p and T denote density, specific heat and temperature and the subscript i either indicates the fluid (f) or the solid (s) phase. In order to obtain an exact solution of the heat conduction problem, Eq. (140) would have to be solved together with appropriate continuity conditions on the solid/fluid interface. Clearly, this is an unmanageable task for macroscopic material samples with a complex pore structure.

Following the line of arguments developed by Carbonell and Whitaker [188] and Nozad et al. [189], a volume-averaged temperature is introduced as

$$\langle T \rangle_i = \frac{1}{V_i} \int_{V_i} T \, \mathrm{d}V \,, \tag{141}$$

where the subscript i indicates either fluid or solid and the integral is either over the fluid or the solid volume embraced by the averaging volume shown in Figure 2.67. One proceeds by averaging Eq. (140) over the fluid or solid volume, depending on which phase is considered. In addition, the temperature field is split into a mean value (defined by the local averaging procedure) and a fluctuating component, according to

$$T_i = \langle T \rangle_i + T_i' \,. \tag{142}$$

Assuming local thermal equilibrium, i.e. the equality of the averaged fluid and solid temperature, a transport equation for the average temperature results which still contains and integral over the fluctuating component. In order to close the equation, a relationship between the fluctuating component and the spatial derivatives of the average temperature of the form

$$T_i' = (b_i)_k \frac{\partial \langle T \rangle}{\partial x_k} \tag{143}$$

is assumed, where the transformation vector $(b_i)_k$ might depend on the spatial coordinates. With that assumption a diffusion equation for the average temperature can be derived, given as

$$\left[\varepsilon (\rho\, c_p)_\mathrm{f} + (1 - \varepsilon)\, (\rho\, c_p)_\mathrm{s} \right] \frac{\partial \langle T \rangle}{\partial t} = \frac{\partial}{\partial x_k} \left[(\Lambda_\mathrm{e})_{kl} \frac{\partial \langle T \rangle}{\partial x_l} \right]. \tag{144}$$

The effective thermal conductivity tensor Λ_e depends on the transformation vector $(b_i)_k$ introduced above and on the geometry of the pore space. Hence, under the assumptions made, heat conduction in a porous medium is described by an effective transport coefficient matrix Λ_e. Similarly, for mass transfer and flow effective transport equations may be derived using the volume-averaging approach. In such a way, the well-known Darcy equation for flow in porous media may be obtained [190]:

$$\langle u_k \rangle = -\frac{K}{\mu} \frac{\partial p}{\partial x_k}, \tag{145}$$

where $\langle u_k \rangle$ denotes the average velocity, K the permeability of the medium, μ the fluid viscosity and p pressure.

2.9.3 Computation of Transport Coefficients

In order to be useful in practice, the effective transport coefficients have to be determined for a porous medium of given morphology. For this purpose, a broad class of methods is available (for an overview, see [191]). A very straightforward approach is to assume a periodic structure of the porous medium and to compute numerically the flow, concentration or temperature field in a unit cell [117]. Two very general and powerful methods are the *effective-medium approximation* (EMA) and the *position-space renormalization group method*.

The EMA method is similar to the volume-averaging technique in the sense that an effective transport coefficient is determined. However, it is less empirical and more general, an assessment that will become clear in a moment. Taking mass diffusion as an example, the fundamental equation to solve is

$$\frac{\partial c}{\partial t} = \frac{\partial}{\partial x_\mathrm{k}} \left(D \frac{\partial c}{\partial x_\mathrm{k}} \right), \tag{146}$$

where c is the concentration field and D the diffusivity. Following the derivation given in [191], a grid is introduced with nodes i, j connected by bonds which are characterized by transport coefficients W_{ij} being proportional to the local diffusivity between i and j. The bonds represent the pore throats and the transport coefficients W_{ij} reflect the geometry of the pore throats, for example a very narrow pore

will have assigned a very small value of W_{ij}. Implemented on such a grid, Eq. (146) translates to

$$\frac{\partial c_i}{\partial t} = \sum_j W_{ij} \left[c_i(t) - c_j(t) \right] , \tag{147}$$

where c_i is the concentration at node i. The initial concentration is assumed to be of the form $c_i(t = 0) = c_0 \, \delta_{i0}$. Taking the Laplace transform of Eq. (147), one obtains

$$\omega \, \tilde{c}_i(\omega) - \delta_{i0} = \sum_j W_{ij} \left[\tilde{c}_j(\omega) - \tilde{c}_i(\omega) \right] , \tag{148}$$

where ω is the variable conjugate to t and the tilde indicates a transformed function. The essential idea of the EMA method is to introduce a node independent, but generally ω-dependent, transport coefficient which represents the average properties of the medium, according to

$$\omega \, \tilde{c}_i^e(\omega) - \delta_{i0} = \sum_j \tilde{W}_e(\omega) \left[\tilde{c}_j^e(\omega) - \tilde{c}_i^e(\omega) \right] , \tag{149}$$

where $\tilde{c}_i^e(\omega)$ is the Laplace transform of the effective concentration field obtained in the medium described by the effective transport coefficient. By subtracting Eq. (148) from Eq. (149), an equation involving both $\tilde{c}_i(\omega)$ and $\tilde{c}_i^e(\omega)$ is obtained. When solving this equation approximately and demanding

$$\left\langle \tilde{c}_i(\omega) \right\rangle = \tilde{c}_i^e(\omega) , \tag{150}$$

where the average is defined with respect to a specific probability distribution for W_{ij}, the function $\tilde{W}_e(\omega)$ can be determined. When computing an effective diffusivity from the transport coefficient and translating the results obtained on a grid to a continuum model, a diffusion equation with a memory term is obtained:

$$\frac{\partial c(x_k, t)}{\partial t} = \int_0^\infty D_e(t - \tau) \, \nabla^2 \, c(x_k, \tau) \, \mathrm{d}\tau . \tag{151}$$

The effective diffusivity depends on the statistical distribution of the pore transport coefficients W_{ij}. The derivation shows that the semi-empirical volume-averaging method can only be regarded as an approximation to a more complex dynamic behavior which depends non-locally on the history of the system. Under certain circumstances the long-time ($t \to \infty$) diffusivity will not depend on t (for further details, see [191]). In such a case, the usual Fick diffusion scenario applies. The derivation presented above can, with minor revisions, be applied to the problem of flow in porous media. When considering the heat conduction problem, however, some new aspects have to be taken into account, as heat is transported not only inside the pore space, but also inside the solid phase.

As a second method to determine effective transport coefficients in porous media, the position-space renormalization group method will be briefly discussed.

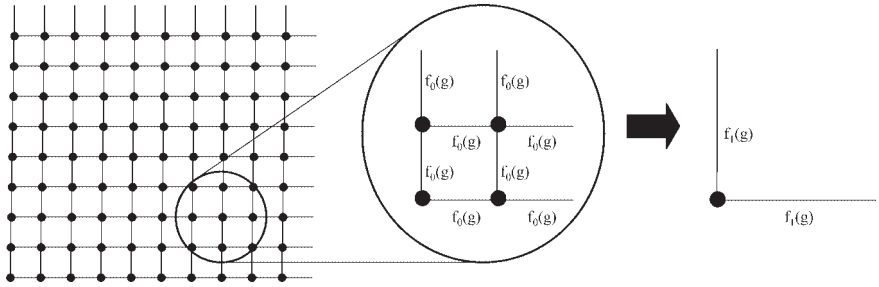

Figure 2.68 Grid model of a porous medium (left) and renormalization group transformation replacing a cluster of grid cells by a unit cell of larger scale (right).

Consider, as an example, a porous medium represented by the two-dimensional grid shown in Figure 2.68, where each bond stands for a pore throat and the coordination number is 4. To each bond a transport coefficient ('conductance') is assigned, similar to the coefficients W_{ij} appearing in the previous paragraph. The transport coefficients are not equal, but are sampled from a probability distribution $f_0(g)$ characteristic of the porous medium under consideration. The idea is to successively replace the fine grid shown on the left of Figure 2.68 by a series of coarser grids which mimic the fine grid as far as the transport properties are concerned. This replacement is indicated on the right of Figure 2.68, going along with the task of determining a new probability distribution $f_1(g)$. In case the relationship between $f_0(g)$ and $f_1(g)$ is simple enough this mapping can be iterated until a grid with cells on a macroscopic scale is reached or, alternatively, until the probability distribution for the transport coefficients remains invariant under a further scale transformation.

Formally, the expression one allowing to compute the probability distribution for a bond of the renormalized cell shown on the right of Figure 2.68 is

$$f_1(g) = \int f_0(g_1)\,\mathrm{d}g_1\; f_0(g_2)\,\mathrm{d}g_2 \ldots f_0(g_n)\,\mathrm{d}g_n\; \delta(g - g') \,. \tag{152}$$

In this expression, the integral is over the conductances of the bonds of the original cell, which, when assigned values g_1, g_2, ..., g_n, result in a conductivity g' of a bond in the renormalized cell. The problem of finding g' can be regarded as the problem of determining the conductivity of an electric circuit, where, taking the example of Figure 2.68, the clamps are arranged either horizontally (for the horizontal bond of the renormalized cell) or vertically (for the vertical bond). Usually, for not too large unit cells, g' is a comparatively simple function of g_i ($i = 1, \ldots, n$). Clearly, for reasons of symmetry the horizontal bonds in Figure 2.68 are equivalent to the vertical ones and the same probability distribution is found for each type of bond in the renormalized cell. Since the renormalized cell is of the same structure as the cells of the original grid, the mapping defined in Eq. (152) can be applied over and over again until, e.g., an invariant probability distribution $f_i(g)$ is obtained.

Although in principle a powerful and elegant method, the position-space renormalization group method yields very complex expressions for the renormalized

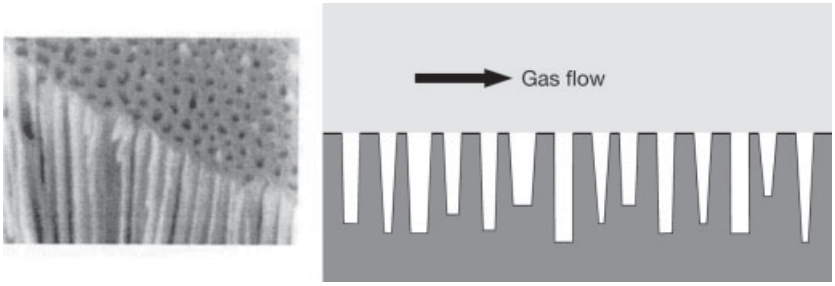

Figure 2.69 Structure of a porous micro channel surface (left) and schematic diagram of the flow scheme and pore arrangement (right).

probability distribution $f_i(g)$ when iterated a few times. Even when using symbolic algebra packages, the number of terms generated soon starts to exceed the capabilities of most computers. For this reason, the probability distribution is often replaced by a distribution of predetermined structure which approximates the true distribution [191]. With such so-called optimized distributions an initial distribution $f_0(g)$ usually converges rapidly to a stable distribution whose shape does not change under further rescaling.

In addition to the approaches for modeling transport phenomena in porous media briefly discussed here, a large number of alternative methods with specific advantages for specific applications exist. An appropriate discussion of only the most important methods lies beyond the scope of this book. The reader is referred to the books by Sahimi [191] and Kaviany [117] for a more detailed presentation of models for flow, heat and mass transfer in porous media. Nevertheless, one further class of modeling approaches which is of special importance for micro reactors should be discussed here. A special class of catalytic surface described in the literature is a monolith with more or less regular, straight and parallel pores [192, 193]. The walls of micro channels may be equipped with such monoliths in order to increase the specific surface area and the number of active sites catalyzing chemical reactions. A microscopic image of a corresponding channel surface is displayed in Figure 2.69, together with the typical flow scheme in corresponding reactors. Corresponding pore structures can be created by anodic oxidation, an electrochemical process in the course of which spots of Al_2O_3 are created on an aluminum substrate.

2.9.4
Reaction-diffusion Dynamics Inside Pores

The simple pore structure shown in Figure 2.69 allows the use of some simplified models for mass transfer in the porous medium coupled with chemical reaction kinetics. An overview of corresponding modeling approaches is given in [194]. The reaction-diffusion dynamics inside a pore can be approximated by a one-dimensional equation

$$\frac{\mathrm{d}^2 c_i}{\mathrm{d}z^2} = \frac{2}{D_i\,\overline{r}}\,\frac{\mathrm{d}n_i}{S_{\mathrm{cat}}\,\mathrm{d}t}\,, \tag{153}$$

where time independence of the concentration profile was assumed. The concentration of species i is denoted by c_i, z is the coordinate along the axis of the pore, D_i the species diffusion constant inside the pore, $\overline{r}$ the mean radius of the pore, n_i the number of moles of species i and S_{cat} the surface area of the catalyst material. The second factor on the right-hand side is the reaction rate per unit surface area of the catalyst material. In order for Eq. (153) to be applicable, the radial concentration gradients inside the pore should be negligible. This condition can be expressed mathematically as [194]

$$\sum_i \frac{\overline{r}}{3\,\nu_i\,D_i}\,\frac{1}{S_{\mathrm{cat}}}\,\frac{\partial(\mathrm{d}n_i/\mathrm{d}t)}{\partial c_i} << 1\,, \tag{154}$$

where ν_i is the stoichiometric coefficient of species i in the chemical reaction under consideration. Assuming a reaction of the type $\mathrm{A} \rightarrow \mathrm{B}$, Eq. (153) can be solved for all reaction orders. The functional forms of the solutions are given in [194] and allow the diffusional flux of species i at the pore mouth to be expressed as a function of concentration.

When modeling the reaction dynamics in micro channels equipped with such porous walls, the arguments outlined above allow the computations to be simplified considerably. Given the applicability of the one-dimensional approximation for the reaction-diffusion dynamics inside the pores, the domain of the catalyst monolith does no longer have to be included explicitly in the computational model. Consider, for example, a CFD model of a reactor with gas flow past a catalyst monolith with regular, parallel pores, such as depicted in Figure 2.69. It would be very challenging in terms of CPU time and memory requirements to include the pore space into the computational domain and define a grid inside the pores which would have to be matched with the grid of the flow channel. Rather than that, the techniques discussed above allow one to define the interface between the catalyst monolith and the channel as the boundary of the computational domain, similar to a smooth, unstructured surface acting as catalyst. The flow, heat and mass transfer problem would then only be solved in a computational domain defined by the flow channel. In such a model, the diffusional fluxes of chemical species at the interface to the monolith would be related to the concentrations via the relations for various reaction orders derived from the one-dimensional pore transport model, Eq. (153). However, when employing such an approach care has to be taken that all conditions allowing neglect of the catalyst domain in an explicit model are fulfilled. As an example, the temperature boundary condition at the interface to the monolith may *a priori* not be clear and heat conduction effects inside the porous medium might have to be taken into account.

References

1 Pope, S. B., *Turbulent Flows,* Cambridge University Press, Cambridge (**2000**).

2 Karniadakis, G. E., Beskok, A., *Micro Flows – Fundamentals and Simulation,* Springer-Verlag, New York (**2002**).

3 Gad-el-Hak, M., *The fluid mechanics of microdevices,* J. Fluids Eng. **121** (**1999**) 5–33.

4 Bird, G., *Molecular Gas Dynamics and the Direct Simulation of Gas Flows,* Oxford University Press, New York (**1994**).

5 Schaaf, S., Chambre, P., *Flow of Rarified Gases,* Princeton University Press, Princeton, NJ (**1961**).

6 Seidl, M., Steinheil, E., *Measurement of momentum accomodation coefficients on surfaces characterized by Auger spectroscopy, SIMS and LEED,* in Proceedings of the 9th Int. Symposium on Rarified Gas Dynamics, pp. E9.1–E9.2 (**1974**).

7 Lord, R., *Tangential momentum coefficients of rare gases on polycrystalline surfaces,* in Proceedings of the 10th Int. Symposium on Rarified Gas Dynamics, pp. 531–538 (**1976**).

8 Beskok, A., Karniadakis, G. E., *Simulation of heat and momentum transfer in complex micro-geometries,* J. Thermophys. Heat Transfer **8** (**1994**) 355–370.

9 Tu, J. K., Huen, T., Szema, R., Ferrari, M., *Filtration of sub-100 nm particles using a bulk-micromachined, direct-bonded silicon filter,* J. Biomed. Microdevices **1** (**1999**) 113–119.

10 Han, J., Craighead, H. G., Separation of long DNA molecules in a microfabricated trap array, *Science* **288** (**2000**) 1026–1029.

11 Han, J., Craighead, H. G., *Characterization and optimization of an entropic trap for DNA separation,* Anal. Chem. **74** (**2002**) 394–401.

12 Foquet, M., Korlach, J., Zipfel, W., Webb, W. W., Craighead, H. G., *DNA fragment sizing by single molecule detection in submicrometer-sized closed fluidic channels,* Anal. Chem. **74** (**2002**) 1415–1422.

13 Zapf, R., Berresheim, K., Cominos, V., Gnaser, H., Hessel, V., Kolb, G., Löb, P., *Detailed characterization of various porous alumina based catalyst coatings within microchannels and their testing for methanol steam reforming,* Chem. Eng. Res. Des., special issue on Chemical Reaction Engineering (**2003**) submitted for publication.

14 Haas-Santo, K., Fichtner, M., Schubert, K., *Preparation of microstructure compatible porous supports by sol–gel synthesis for catalyst coatings,* Appl. Catal. A **220** (**2001**) 79–92.

15 Reif, F., *Fundamentals of Statistical and Thermal Physics,* McGraw-Hill, New York (**1965**).

16 Bhatnager, P., Gross, E., Krook, K., *A model for collision processes in gases,* Phys. Rev. **94** (**1954**) 511–524.

17 Cercignani, C., *The Boltzmann Equation and its Applications,* Springer-Verlag, New York (**1988**).

18 Cercignani, C., *Rarified Gas Dynamics: From Basic Concepts to Actual Calculations,* Cambridge University Press, New York (**2000**).

19 Chapman, S., Cowling, T., *The Mathematical Theory of Non-uniform Gases: An account of the Kinetic Theory of Viscosity, Thermal Conduction and Diffusion in Gases,* Cambridge University Press, Cambridge (**1970**).

20 Sharipov, F., Sleznev, V., *Data on internal rarified gas flows,* J. Phys. Chem. Ref. Data **27** (**1998**) 657–706.

21 Sharipov, F., Kalempa, D., *Gaseous mixture flow through a long tube at arbitrary Knudsen numbers,* J. Vac. Sci. Technol. A **20** (**2002**) 814–822.

22 Oh, C. K., Oran, E. S., Sinkovits, R. S., *Computations of high-speed, high Knudsen number microchannel flow,* J. Thermophys. Heat Transfer **11**, 4 (**1997**) 497–505.

23 Cai, C., Boyd, I. D., Fan, J., Candler, G. V., *Direct simulation methods for low-speed microchannel flows,* J. Thermophys. Heat Transfer **14**, 3 (**2000**) 368–378.

24 Kaplan, C. R., Oran, E. S., *Nonlinear filtering for low-velocity gaseous microflows,* AIAA J. **40** (**2002**) 82–90.

25 Fan, J., Chen, C., *Statistical simulation of low-speed unidirectional flows in transitional*

regime, in Brun, R. C. E. (Ed.), *Rarified Gas Dynamics,* Cepadues Editions, Toulouse, Vol. 2, pp. 245–252 (**1999**).

26 Sun, H., Faghri, M., *Effect of surface roughness on nitrogen flow in a microchannel using the Direct Simulation Monte Carlo Method (DSMC),* Numerical Heat Transfer A **43** (**2003**) 1–8.

27 Roveda, R., Goldstein, D., Varghese, P., *Hybrid Euler/particle approach for continuum/rarified flows.* J. Spacecraft Rockets **35** (**1998**) 258–265.

28 Atkas, O., Aluru, N. R., *A combined continuum/DSMC technique for multiscale analysis of microfluidic filters,* J. Comput. Phys. **178**, 2 (**2000**) 342–372.

29 Landau, L. D., Lifshitz, E. M., *Hydrodynamik,* Akademie-Verlag, Berlin (**1991**).

30 Wrobel, L. C., *The Boundary Element Method,* Wiley, New York (**2002**).

31 Pfahler, J., Harley, J., Bau, H., Zemel, J., *Liquid transport in micron and submicron channels,* Sens. Actuators A **21–23** (**1990**) 431–434.

32 Peng, X. F., Peterson, G. P., Wang, B. X., *Frictional flow characteristics of water flowing through rectangular microchannels,* Exp. Heat Transfer **7** (**1994**) 249–264.

33 Peng, X. F., Peterson, G. P., *The effect of thermofluid and geometrical parameters on convection of liquids through rectangular microchannels,* Int. J. Heat Mass Transfer **38**, 4 (**1995**) 755–758.

34 Flockhart, S. M., Dhariwal, R. S., *Experimental and numerical investigation into the flow characteristics of channels etched in (100) silicon,* J. Fluids Eng. **120** (**1998**) 291–295.

35 Harms, T. M., J., K. M., Gerner, F. M., *Developing convective heat transfer in deep rectangular microchannels,* Int. J. Heat Fluid Flow **20** (**1999**) 149–157.

36 Mala, G. M., Li, D., *Flow characteristics of water in microtubes,* Int. J. Heat Fluid Flow **20** (**1999**) 142–148.

37 Qu, W., Mala, G. M., Li, D., *Pressure-driven water flows in trapezoidal silicon microchannels,* Int. J. Heat Mass Transfer. **43** (**2000**) 353–364.

38 Brochard, F., de Gennes, P. G., *Shear-dependent slippage at a polymer/solid interface,* Langmuir **8** (**1992**) 3033–3037.

39 Migler, K. B., Hervet, H., Leger, L., *Slip transition of a polymer melt under shear stress,* Phys. Rev. Lett. **70** (**1993**) 287–290.

40 Baudry, J., Charlaix, E., Tonck, A., Mazuyer, D., *Experimental evidence for a large slip effect at a nonwetting fluid-solid interface,* Langmuir **17** (**2001**) 5232–5236.

41 Craig, V. S. J., Neto, C., Williams, D. R. M., *Shear-dependent boundary slip in an aqueous Newtonian liquid,* Phys. Rev. Lett. **87** (**2001**) 54504–54507.

42 Bonaccurso, E., Kappl, M., Butt, H. J., *Hydrodynamic force measurements: boundary slip of water on hydrophilic surfaces and electrokinetic effects,* Phys. Rev. Lett. **88** (**2002**) 76103–76106.

43 Thompson, P. A., Troian, S. M., *A general boundary condition for liquid flow at solid surfaces,* Nature **389** (**1997**) 360–362.

44 Ashcroft, N. W., Mermin, N. D., *Solid State Physics,* Harcourt Brace College Publishers, Fort Worth, TX (**1976**).

45 Probstein, R. F., *Physicochemical Hydrodynamics,* Wiley, New York (**1994**).

46 Rice, C., Whitehead, R., *Electro kinetic flow in a narrow cylindrical capillary,* J. Phys. Chem. **69** (**1965**) 4017–4023.

47 Adamson, A. W., Gast, A. P., *Physical Chemistry of Surfaces,* 6th ed., Wiley, New York (**1997**).

48 Zeng, S., Chen, C. H., Mikkelsen, J. C., Santiago, J. G., *Fabrication and characterization of electroosmotic micropumps,* Sens. Actuators B **79** (**2001**) 107–114.

49 Chen, C. H., Santiago, J. G., *A planar electroosmotic micropump,* J. Microelectromech. Syst. **11** (**2002**) 672–683.

50 Lazar, I. M., Karger, B. M., *Multiple open-channel electroosmotic pumping system for microfluidic sample handling,* Anal. Chem. **74** (**2002**) 6259–6268.

51 Burgreen, D., Nakache, F., *Electrokinetic flow in ultrafine capillary slits,* J. Phys. Chem. **68** (**1964**) 1084–1091.

52 Hunter, R. J., *Zeta Potential in Colloid Science: Principles and Applications,* Academic Press, New York (**1981**).

53 Yang, C., Li, D., Masliyah, J. H., *Modeling forced liquid convection in rectangular microchannels with*

electrokinetic effects, Int. J. Heat Mass Transfer **41** (**1998**) 4229–4249.

54 Cheng, L., Fenter, P., Nagy, K. L., Schlegel, M. L., Sturchio, N. C., *Molecular-scale density oscillations in water adjacent to a mica surface,* Phys. Rev. Lett. **87**, 15 (**2001**) 6103–6104.

55 Travis, K. P., Gubbins, K. E., *Poiseuille flow of Lennard–Jones fluids in narrow slit pores,* J. Chem. Phys. **112**, 4 (**2000**) 1984–1994.

56 Qiao, R., Aluru, N. R., *Ion concentrations and velocity profiles in nanochannel electroosmotic flows,* J. Chem. Phys. **118**, 10 (**2003**) 4692–4701.

57 Koplik, J., Banavar, J. R., *Continuum deductions from molecular hydrodynamics,* Ann. Rev. Fluid Mech. **27** (**1995**) 257–292.

58 Allen, M., Tildesley, D., *Computer Simulations of Liquids,* Clarendon Press, Oxford (**1994**).

59 Nakano, A., Kalia, R. K., Vashishta, P., Campbell, T. J., Ogata, S., Shimojo, F., Saini, S., *Scalable atomistic simulation algorithms for materials research,* Sci. Programming **10**, 4 (**2002**) 263–270.

60 Palm, B., *Heat transfer in microchannels,* Microscale Therm. Eng. **5** (**2001**) 155–175.

61 Peng, C. F., Wang, B. X., *Forced convection and flow boiling heat transfer for liquid flowing through microchannels,* Int. J. Heat Mass Transfer **36** (**1993**) 3421–3427.

62 Peng, X. F., Wang, B. X., *Cooling characteristics with microchanneled structures,* J. Enhanced Heat Transfer **1** (**1994**) 315–326.

63 Peng, X. F., Wang, B. X., *Experimental investigation of heat transfer in flat plates with rectangular microchannels,* Int. J. Heat Mass Transfer **38** (**1995**) 127–137.

64 Goldenfeld, N., *Lectures on Phase Transitions and the Renormalization Group,* Addison Wesley, Boston (**1992**).

65 Toda, M., Kubo, R., Saitô, N., *Statistical Physics I: Equilibrium Statistical Mechanics,* Springer-Verlag, Berlin (**1992**).

66 Fisher, M. E., Nakanishi, H., *Scaling theory for the criticality of fluids between plates,* J. Chem. Phys. **75** (**1981**) 5857–5863.

67 Evans, P., Marconi, U., Tarazona, P., *Fluids in narrow pores: adsorption, capillary condensation and critical points,* J. Chem. Phys. **84** (**1986**) 2376–2399.

68 Krech, M., *Casimir forces in binary liquid mixtures,* Phys. Rev. E **56** (**1997**) 1642–1659.

69 Jacobs, D. T., Mockler, R. C., O'Sullivan, W. J., *Critical-temperature and coexistence-curve measurements in thick films,* Phys. Rev. Lett. **37** (**1976**) 1471–1474.

70 de Gennes, P. G., *Wetting: statics and dynamics,* Rev. Mod. Phys. **57** (**1985**) 827–863.

71 Joanny, J. F., de Gennes, P. G., *A model for contact angle hysteresis,* J. Chem. Phys. **81** (**1984**) 552–562.

72 de Gennes, P. G., Hua, X., Levinson, P., *Dynamics of wetting: local contact angles,* J. Fluid. Mech. **212** (**1990**) 55–63.

73 de Gennes, P. G., *Deposition of Langmuir-Blodgett layers,* J. Colloid Polym. Sci. **264**, 463–465.

74 Cox, R. G., *The dynamics of the spreading of liquids on a solid surface. Part 1. Viscous flow,* J. Fluid. Mech. **168** (**1986**) 169–194.

75 Hlavacek, V., Puszynski, J. A., Viljoen, H. J., Gatica, J. E., *Model reactors and their design equations,* in Arpe, H. J. (Ed.), *Ullmann's Encyclopedia of Industrial Chemistry,* Wiley, New York, Vol. B4, pp. 121–165 (**1992**).

76 Fletcher, C. A. J., *Computational Techniques for Fluid Dynamics,* 2nd ed., Springer-Verlag, Berlin (**1991**).

77 Gresho, P. M., Sani, R. L., *Incompressible Flow and the Finite Element Method, Volume 1: Advection-Diffusion and Isothermal Laminar Flow,* Wiley, New York (**2000**).

78 Gresho, P. M., Sani, R. L., Engelman, M. S., *Incompressible Flow and the Finite Element Method, Volume 2, Isothermal Laminar Flow,* Wiley, New York (**2000**).

79 Versteeg, H. K., Malalasekra, M., *An Introduction to Computational Fluid Dynamics,* Longman Scientific & Technical, Harlow (**1995**).

80 Courant, R., Hilbert, D., *Methoden der Mathematischen Physik,* Springer-Verlag, Berlin (**1993**).

81 Noll, B., *Numerische Strömungsmechanik,* Springer-Verlag, Berlin (**1993**).

82 Leonard, B. P., *A stable and accurate convection modeling procedure based on quadratic upstream interpolation,* Comput. Methods Appl. Mech. Eng. **19** (**1979**) 59–98.

83 Casey, M., Wintergerste, T., *Special Interest Group on Quality and Trust in Industrial CFD: Best Practice Guidelines,* European Research Community on Flow, Turbulence and Combustion (**2000**).

84 Ferziger, J. H., Peric, M., *Computational Methods for Fluid Dynamics,* 3rd ed., Springer-Verlag, Berlin (**2002**).

85 Press, W. H., Teukolsky, S. A., Vetterling, W. T., Flannery, B. P., *Numerical Recipes in Fortran 77,* Cambridge University Press, Cambridge (**1992**).

86 Harlow, F. H., Welsh, J. E., *Numerical calculation of time dependent viscous incompressible flow with free surface,* Phys. Fluids **8** (**1965**) 2182–2189.

87 Rhie, C. M., Chow, W. L., *Numerical study of the turbulent flow past an airfoil with trailing edge separation,* AIAA J. **21** (**1983**) 1527–1532.

88 Caretto, L. S., Gosman, A. D., Patankar, S. V., Spalding, D. B., *Two calculation procedures for steady, three-dimensional flows with recirculation,* in Proceedings of the 3rd Int. Conf. Numer. Methods Fluid Dyn., Paris (**1972**).

89 van Doormal, J. P., Raithby, G. D., *Enhancement of the SIMPLE method for predicting incompressible fluid flows,* Numerical Heat Transfer **7** (**1984**) 147–163.

90 Gerritsen, M., Olsson, P., *Designing an efficient solution strategy for fluid flows. II. Stable high-order central finite difference schemes on composite adaptive grids with sharp shock resolution,* J. Comput. Phys. **147** (**1998**) 293–317.

91 Kinoshita, T., Inoue, O., *A parallel adaptive mesh approach for flowfields with shock waves,* Shock Waves **12** (**2002**) 167–175.

92 Becker, R., Rannacher, R., *A feedback approach to error control in finite element methods: basic analysis and examples,* East-West J. Numer. Math. **4** (**1996**) 237–264.

93 Heuveline, V., Rannacher, R., *A posteriori error control for finite element approximations of elliptic eigenvalue problems,* Adv. Comp. Math. **15** (**2001**) 107–138.

94 Thompson, J. F., Warsi, Z. U., Mastin, C. W., *Boundary-fitted coordinate systems for numerical solution of partial differential equations,* J. Comput. Phys. **47** (**1982**) 1–108.

95 Lo, S. H., *A new mesh generation scheme for arbitrary planar domains,* Int. J. Num. Methods Eng. **21** (**1985**) 1403–1426.

96 Thompson, J. F., Soni, B. K., Weatherill, N. P., *Handbook of Grid Generation,* CRC Press, Boca Raton, FL (**1998**).

97 Trottenberg, U., Oosterlee, C. W., Schüller, A., *Multigrid,* Academic Press, New York (**2001**).

98 Stoer, J., Bulirsch, R., *Introduction to Numerical Analysis,* Springer-Verlag, New York (**1980**).

99 Briggs, W. L., Henson, V., McCromick, S. F., *A Multigrid Tutorial, 2nd ed.,* Society for Industrial and Applied Mathematics, Philadelphia (**2000**).

100 Hartnett, J. P., Kostic, M., *Heat transfer to Newtonian and non-Newtonian fluids in rectangular ducts,* Adv. Heat Transfer **19** (**1989**) 247–356.

101 Purday, H. F. P., *An Introduction to the Mechanics of Viscous Flow,* Dover, New York (**1949**).

102 Shah, R. K., London, A. L., *Laminar flow forced convection in ducts,* Adv. Heat Transfer Suppl. 1 (**1978**).

103 Shah, R. K., *Laminar flow friction and forced convection heat transfer in ducts of arbitrary geometry,* Int. J. Heat Mass Transfer **18** (**1975**) 849–842.

104 Richardson, D. H., Sekulic, D. P., Campo, A., *Low Reynolds number flow inside straight micro channels with irregular cross sections,* Heat Mass Transfer **36** (**2000**) 187–193.

105 Asako, Y., Faghri, M., *Finite-volume solutions for laminar flow and heat transfer in a corrugated duct,* J. Heat Transfer **109** (**1987**) 627–634.

106 Garg, V. K., Maji, P. K., *Flow and heat transfer in a sinusoidally curved channel,* Int. J. Eng. Fluid Mech. **1** (**1988**) 293–319.

107 Guzmán, A. M., Amon, C. H., *Dynamical flow characterization of*

transitional and chaotic regimes in converging–diverging channels, J. Fluid. Mech. **321** (**1996**) 25–57.

108 Dean, W. R., *Note on the motion of a fluid in a curved pipe,* Philos. Mag. **4** (**1927**) 208–223.

109 Dean, W. R., *The stream-line motion of fluid in a curved pipe,* Philos. Mag. **5** (**1928**) 673–695.

110 Cheng, K. C., Lin, R.-C., Ou, J.-W., *Fully developed laminar flow in curved rectangular channels,* J. Fluids Eng. **3** (**1976**) 42–48.

111 Chen, Y., Chen, P., *Heat transfer and pressure drop in fractal tree-like microchannel nets,* Int. J. Heat Mass Transfer **45** (**2002**) 2643–2648.

112 Walter, S., Frischmann, G., Broucek, R., Bergfeld, M., Liauw, M., *Fluiddynamische Aspekte in Mikroreaktoren,* Chem. Ing. Tech. **71**, 5 (**1999**) 447–455.

113 Cominos, V., Hardt, S., Hessel, V., Kolb, G., Löwe, H., Wichert, M., Zapf, R., *A methanol steam micro-reformer for low power fuel cell applications,* Chem. Eng. Commun. (**2003**) accepted for publication.

114 Verfürth, R., *Non-overlapping domain decomposition methods,* in Bristeau, M. O., Etgen, G. J., Fitzgibbon, W., Lions, J. L., Periaux, J., Wheeler, M. F. (Eds.), *Computational Science for the 21st Century,* Wiley, New York (**1997**).

115 Ewing, R., Lazarov, R., Lin, T., Lin, Y., *Mortar finite volume element approximations of second order elliptic problems,* East-West J. Numer. Math. **8**, 2 (**2000**) 93–110.

116 Commenge, J. M., Falk, L., Corriou, J. P., Matlosz, M., *Optimal design for flow uniformity in microchannel reactors,* AIChE J. **48**, 2 (**2000**) 345–358.

117 Kaviany, M., *Principles of Heat Transfer in Porous Media,* Springer-Verlag, New York (**1995**).

118 Kim, S. J., Kim, D., Lee, D. Y., *On the local thermal equilibrium in microchannel heat sinks,* Int. J. Heat Mass Transfer **43** (**2000**) 1735–1748.

119 White, F. M., *Fluid Mechanics,* McGraw-Hill, New York (**1994**).

120 Hardt, S., Ehrfeld, W., Hessel, V., vanden Bussche, K. M., *Strategies for size reduction of microreactors by heat transfer enhancement effects,* Chem. Eng. Commun. **190**, 4 (**2003**) 540–559.

121 Rush, T. A., Newell, T. A., Jacobi, A. M., *An experimental study of flow and heat transfer in sinusoidal wavy passages,* Int. J. Heat Mass Transfer **42** (**1999**) 1541–1553.

122 Wang, G., Vanka, S. P., *Convective heat transfer in periodic wavy passages,* Int. J. Heat Mass Transfer **38** (**1995**) 3219–3230.

123 Sekulic, D. P., Campo, A., Morales, J. C., *Irreversibility phenomena associated with heat transfer and fluid friction in laminar flows through singly connected ducts,* Int. J. Heat Mass Transfer **40** (**1997**) 905–914.

124 Xu, B., Ooi, K. T., Mavriplis, C., Zaghloul, M. E., *Evaluation of viscous dissipation in liquid flow in microchannels,* J. Micromech. Microeng. **13** (**2003**) 53–57.

125 Stief, T., Langer, O.-U., Schubert, K., *Numerical investigations of opimal heat conductivity in micro heat exchangers,* Chem. Eng. Technol. **21**, 4 (**1999**) 297–302.

126 Perry, R. H., Green, D. W., *Perry's Chemical Engineers' Handbook,* 7th ed., McGraw-Hill, New York (**1997**).

127 Drese, K.-S., Hardt, S., *Characterization of micro heat exchangers,* in Proceedings of the VDE World Microtechnologies Congress, MICRO.tec 2000 (25–27 September **2000**), VDE Verlag, Berlin, EXPO Hannover, pp. 371–374.

128 Quiram, D. J., Hsing, I.-M., Franz, A. J., Jensen, K. F., Schmidt, M. A., *Design issues for membrane-based, gas phase microchemical systems,* Chem. Eng. Sci. **55** (**2000**) 3065–3075.

129 Brooks, A. N., Hughes, T. J. R., *Streamline upwind Petrov/Galerkin formulation for convection dominated flows with particular emphasis on the incompressible Navier–Stokes equations,* Comput. Methods Appl. Mech. Eng. **32** (**1982**) 99–259.

130 Quiram, D. J., Hsing, I.-M., Franz, A. J., Srinivasan, R., Jensen, K. F., Schmidt, M. A., *Characterization of microchemical systems using simulations,* in Ehrfeld, W., Rinard, I. H.,

Wegeng, R. S. (Eds.), *Process Miniaturization: 2nd International Conference on Microreaction Technology, IMRET 2, Topical Conf. Preprints,* AIChE, New Orleans, pp. 205–211 (**1998**).

131 Boris, J. P., Book, D. L., *Flux-corrected transport – I. SHASTA, a fluid transport algorithm that works,* J. Comput. Phys. **11** (**1973**) 38–69.

132 Zalesak, S. T., *Fully multidimensional flux-corrected transport algorithm for fluids,* J. Comput. Phys. **31** (**1979**) 335–362.

133 Ehrfeld, W., Hessel, V., Löwe, H., *Microreactors,* Wiley-VCH, Weinheim (**2000**).

134 Gobby, D., Angeli, P., Gavriilidis, A., *Mixing characteristics of T-type microfluidic mixers,* J. Micromech. Microeng. **11** (**2001**) 126–132.

135 Mengeaud, V., Josserand, J., Girault, H. H., *Mixing processes in a zigzag microchannel: finite element simulations and optical study,* Anal. Chem. **74** (**2002**) 4279–4286.

136 Stroock, A. D., Dertinger, S. K. W., Whitesides, G. M., Ajdari, A., *Patterning flows using grooved surfaces,* Anal. Chem. **74**, 20 (**2002**) 5306–5312.

137 Stroock, A. D., Dertinger, S. K. W., Ajdari, A., Mezic, I., Stone, H. A., Whitesides, G. M., *Chaotic mixer for microchannels,* Science **295**, 1 (**2002**) 647–651.

138 Aref, H., *Stirring by chaotic advection,* J. Fluid. Mech. **143** (**1984**) 1–21.

139 Schönfeld, F., Hardt, S., *Simulation of helical flows in microchannels,* AIChE J. (**2003**) accepted for publication.

140 Linxiang, W., Yurun, F., Ying, C., *Animation of chaotic mixing by a backward Poincaré cell-map method,* Int. J. Bifurcation Chaos **11**, 7 (**2001**) 1953–1960.

141 Hessel, V., Hardt, S., Löwe, H., Schönfeld, F., *Laminar mixing in different interdigital micromixers – Part I: experimental characterization,* AIChE J. **49**, 3 (**2003**) 566–577.

142 Hardt, S., Schönfeld, F., *Laminar mixing in different interdigital micromixers – Part 2: numerical simulations,* AIChE J. **49**, 3 (**2003**) 578–584.

143 Thompson, L. H., Doraiswamy, L. K., *Sonochemistry: science and engineering,* Ind. Eng. Chem. Res. **38** (**1999**) 1215–1249.

144 Qian, S., Bau, H. H., *A chaotic electroosmotic stirrer,* Anal. Chem. **74**, 15 (**2002**) 3616–3625.

145 Meisel, I., Ehrhard, P., *Simulation of electrically-excited flows in microchannels for mixing applications,* in Proceedings of the 5th International Conference on Modeling and Simulation of Microsystems, San Juan, Puerto Rico, 22–25 April 2002, Computational Publications, Boston, pp. 62–65 (**2002**).

146 Bau, H. H., Zhong, J., Yi, M., *A minute magneto hydro dynamic (MHD) mixer,* Sens. Actuators B **79** (**2001**) 207–215.

147 Gleeson, J. P., West, J., *Magnetohydrodynamic mixing,* in Proceedings of the 5th International Conference on Modeling and Simulation of Microsystems, San Juan, Puerto Rico, 22–25 April 2002, Computational Publications, Boston, pp. 318–321 (**2002**).

148 Gleeson, J. P., Roche, O. M., West, J., *Modeling annular micromixers,* in Proceedings of the Nanotechnology Conference and Trade Show, Nanotech 2003, San Francisco, 23–27 February 2003, Computational Publications, Boston, pp. 206–209 (**2003**).

149 Taylor, G. I., *Dispersion of soluble matter in solvent flowing slowly through a tube,* Proc. R. Soc. London, **A 219** (**1953**) 186–203.

150 Aris, R., *On the dispersion of a solute in a fluid flowing through a tube,* Proc. R. Soc. London, **A 235** (**1956**) 67–77.

151 Gill, W. N., Sankarasubramanian, R., *Exact analysis of unsteady convective diffusion,* Proc. R. Soc. London, **A 316** (**1970**) 341–350.

152 Doshi, M. R., Daiya, P. M., Gill, W. N., *Three dimensional laminar dispersion in open and closed rectangular conduits,* Chem. Eng. Sci. **33** (**1978**) 795–804.

153 Dutta, D., Leighton, D. T., *Dispersion reduction in pressure-driven flow through microetched channels,* Anal. Chem. **75**, 1 (**2001**) 57–70.

154 Aris, R., *On the dispersion of a solute by diffusion, convection and exchange between phases,* Proc. R. Soc. London, **A 252** (**1959**) 538–550.

155 Daskopoulos, P., Lenhoff, A. M., *Dispersion coefficient for laminar flow in curved tubes,* AIChE J. **34**, 12 (**1988**) 2052–2058.

156 Thomas, J. M., Thomas, W. J., *Principles and Practice of Heterogeneous Catalysis,* VCH, Weinheim (**1997**).

157 Fedorov, A. G., Viskanta, R., *Heat and mass transfer dynamics in the microchannel adsorption reactor,* Microscale Therm. Eng. **3** (**1999**) 111–139.

158 Maas, U., *Efficient calculation of intrinsic low-dimensional manifolds for the simplification of chemical kinetics,* Comput. Visualization Sci. **1** (**1998**) 69–82.

159 Maas, U., Pope, S. B., *Simplifying chemical kinetics: intrinsic low-dimensional manifolds in composition space,* Combust. Flame **88** (**1992**) 239–264.

160 Kiehl, M., *Partitioning methods for the simulation of fast reactions,* Zentralbl. Angew. Math. Mech. **78** (**1998**) 967–970.

161 Pope, S. B., *Computationally efficient implementation of combustion chemistry using in situ adaptive tabulation,* Combust. Theory Model. **1** (**1997**) 41–63.

162 Gobby, D., Eames, I., Gavriilidis, A., *A vertically-averaged formulation of catalytic reactions in microchannel flows,* in Matlosz, M., Ehrfeld, W., Baselt, J. P. (Eds.), *Microreaction Technology – IMRET 5: Proc. 5th International Conference on Microreaction Technology,* Springer-Verlag, Berlin (**2001**), pp. 141–149.

163 Walker, R. E., *Chemical reaction and diffusion in a catalytic tubular reactor,* Phys. Fluids **4** (**1961**) 1211–1216.

164 Commenge, J. M., Falk, L., Corriou, J. P., Matlosz, M., *Microchannel reactors for kinetic measurement: influence of diffusion and dispersion on experimental accuracy,* in Matlosz, M., Ehrfeld, W., Baselt, J. P. (Eds.), *Microreaction Technology – IMRET 5: Proc. 5th International Conference on Microreaction Technology,* Springer-Verlag, Berlin (**2001**), pp. 131–140.

165 TeGrotenhuis, W. E., King, D. L., Brooks, K. P., J., G. B., Wegeng, R. S., *Optimizing microchannel reactors by trading-off equilibrium and reaction kinetics through temperature management,* in *Proceedings of the 6th International Conference on Microreaction Technology, IMRET 6,* 11–14 March 2002, AIChE Pub. No. 164, New Orleans (**2002**), pp. 18– 28.

166 Rouge, A., Spoetzl, B., Gebauer, K., Schenk, R., Renken, A., *Microchannel reactors for fast periodic operation: the catalytic dehydration of isopropanol,* Chem. Eng. Sci. **56** (**2001**) 1419–1427.

167 Walter, S., Liauw, M., *Fast concentration cycling in microchannel reactors,* in *Proceedings of the 4th International Conference on Microreaction Technology, IMRET 4,* 5–9 March 2000, AIChE Topical Conf. Proc., Atlanta, GA (**2000**), pp. 209–214.

168 Liauw, M., Baerns, M., Broucek, R., Buyevskaya, O. V., Commenge, J.-M., Corriou, J.-P., Falk, L., Gebauer, K., Hefter, H. J., Langer, O.-U., Löwe, H., Matlosz, M., Renken, A., Rouge, A., Schenk, R., Steinfeld, N., Walter, S., *Periodic operation in microchannel reactors,* in Ehrfeld, W. (Ed.), *Microreaction Technology: 3rd International Conference on Microreaction Technology, Proc. of IMRET 3,* Springer-Verlag, Berlin (**2000**), pp. 224–234.

169 Stepanek, F., Kubicek, M., Marek, M., Adler, P. M., *Optimal design and operation of a separating microreactor,* Chem. Eng. Sci. **54** (**1999**) 1494–1498.

170 Saad, Y., Schultz, M. H., *GMRES: a generalized residual algorithm for solving nonsymmetric linear systems,* SIAM J. Sci. Stat. Comput. **7** (**1989**) pp. 856–869.

171 Sommerfeld, M., Tsuji, Y., Crowe, C. T., *Multiphase Flows with Droplets and Particles,* CRC Press, Boca Raton, FL (**1997**).

172 Thé, J. L., Raithby, G. D., Stubley, G. D., *Surface-adaptive finite-volume method for solving free-surface flows,* Numer. Heat Transfer **B26** (**1994**) 367–380.

173 Raithby, G. D., Xu, W. X., Stubley, G. D., *Prediction of incompressible free Surface flows with an element-based finite volume method,* Comput. Fluid Dyn. J. **4** (**1995**) 353–371.

174 Hirt, C. W., Nichols, B. D., *Volume of fluid (VOF) method for dynamics of free boundaries,* J. Comput. Phys. **39** (**1981**) 201–221.

175 CFX4 User Manual, *Surface sharpening in free surface flows,* Ansys CFX.

176 Brackbill, J. U., Kothe, D. B., Zemach, C., *A continuum method for modeling surface tension,* J. Comput. Phys. **100** (**1992**) 335–354.

177 Noh, W. F., Woodward, P. R., *SLIC simple line interface method,* Lect. Notes Phys. **59** (**1976**), pp. 330–340.

178 Rider, W. J., Kothe, D. B., *Reconstructing volume tracking,* J. Comput. Phys. **141** (**1998**) 112–152.

179 Osher, S., Sethian, J. A., *Fronts propagating with curvature-dependent speed: algorithms based on Hamilton–Jacobi formulations,* J. Comput. Phys. **79** (**1988**) 12–49.

180 Zhang, H., Zheng, L. L., Prasad, V., Hou, T. Y., *A curvilinear level set formulation for highly deformable free surface problems with application to solidification,* Numer. Heat Transfer **34** (**1998**) 1–20.

181 Tryggvason, G., Bunner, B., Esmaeeli, A., Juric, D., Al-Rawahdi, N., Tauber, W., Han, J., Nas, S., Jan, Y. J., *A front-tacking method for the computations of multiphase flow,* J. Comput. Phys. **169** (**2001**) 708–759.

182 Hardt, S., Schönfeld, F., Weise, F., Hofmann, C., Ehrfeld, W., *Simulation of droplet formation in micromixers,* in *Proceedings of the 4th International Conference on Modeling and Simulations of Microsystems,* 19–21 March 2001), Hilton Head Island, SC (2001) pp. 223–226.

183 Hardt, S., Schönfeld, F., *Simulation of hydrodynamics in multi-phase micro-reactors,* in *Proceedings of the 5th World Congress on Computional Mechanics, WCCM,* 7–12 July 2002, Vienna (http://wccm.tuwien.ac.at).

184 Eggers, J., *Nonlinear dynamics and breakup of free-surface flows,* Rev. Mod. Phys. **69**, 3 (**1997**) 865–929.

185 Yang, Z. L., Palm, B., Sehgal, B. R., *Numerical simulation of bubbly two-phase flow in a narrow channel,* Int. J. Heat Mass Transfer **45** (**2002**) 631–639.

186 Higuera, F. J., Succi, S., Benzi, R., *Lattice gas dynamics with enhanced collisions,* Europhys. Lett. **9** (**1989**) 345–349.

187 Tryggvason, G., Fernández, A., Lu, J., *The effect of electrostatic forces on droplet suspensions,* in *Proceedings of the Second M.I.T. Conference on Computational Fluid and Solid Mechanics,* June 17–20 2003, M.I.T., Cambridge, MA, Elsevier, Oxford, UK (**2003**), pp. 1166–1168.

188 Carbonell, R. G., Whitaker, S., *Heat and mass transfer in porous media,* in *Fundamentals of Transport Phenomena in Porous Media,* Martinus Nijhoff, Dordrecht (**1984**) pp. 121–198.

189 Nozad, I., Carbonell, R. G., Whitaker, S., *Heat conduction in multi-phase systems I: theory and experiments for two-phase systems,* Chem. Eng. Sci. **40** (**1985**) 843–855.

190 Whitaker, S., *Flow in porous media I: A theoretical derivation of Darcy's Law,* Trans. Porous Media **1** (**1986**) 3–25.

191 Sahimi, M., *Flow and Transport in Porous Media and Fractured Rock,* VCH, Weinheim (**1995**).

192 Wiessmeier, G., Hönicke, D., *Micro-fabricated components for heterogeneously catalyzed reactions,* J. Micromech. Microeng. **6** (**1996**) 285–289.

193 Wunsch, R., Fichtner, M., Schubert, K., *Anodic oxidation inside completely manufactured microchannel reactors made of aluminum,* in *Proceedings of the 4th International Conference on Microreaction Technology, IMRET 4,* 5–9 March 2000, AIChE Topical Conf. Proc., Atlanta, GA (**2000**), pp. 481–487.

194 Xu, Y., Platzer, B., *Concepts for the simulation of wall-catalyzed reactions in microchannel reactors with mesopores in the wall region,* Chem. Eng. Technol. **24**, 8 (**2001**) 773–783.